Physics – Uspekhi **56** (1) 3 – 28 (2013)

REVIEWS OF TOPICAL PROBLEMS PACS numbers: 13.75.Cs, 13.85.Dz

Elastic scattering of hadrons

I M Dremin

DOI: 10.3367/UFNe.0183.201301a.0003

Contents

Abstract. Colliding high-energy hadrons either produce new particles or scatter elastically with their quantum numbers conserved and no other particles produced. We consider the latter case here. Although inelastic processes dominate at high energies, elastic scattering contributes considerably (18–25%) to the total cross section. Its share first decreases and then increases at higher energies. Small-angle scattering prevails at all energies. Some characteristic features can be seen that provide information on the geometrical structure of the colliding particles and the relevant dynamical mechanisms. The steep Gaussian peak at small angles is followed by the exponential (Orear) regime with some shoulders and dips, and then by a power-law decrease. Results from various theoretical approaches are compared with experimental data. Phenomenological models claiming to describe this process are reviewed. The unitarity condition predicts an exponential fall for the differential cross section with an additional substructure to occur exactly between the low momentum transfer diffraction cone and a power-law, hard parton scattering regime under high momentum transfer. Data on the interference of the Coulomb and nuclear parts of amplitudes at extremely small angles provide the value of the real part of the forward scattering amplitude. The real part of the elastic scattering amplitude and the contribution of inelastic processes to the imaginary part of this amplitude (the so-called overlap function) are also discussed. Problems related to the scaling behavior of the differential cross section are considered. The power-law regime at highest momentum transfer is briefly described.

I M Dremin Lebedev Physical Institute, Russian Academy of Sciences, Leninskii prosp. 53, 119991 Moscow, Russian Federation
Tel. +7 (499) 783 37 19. Fax +7 (499) 135 78 80
E-mail: dremin@lpi.ru

Received 18 June 2012
Uspekhi Fizicheskikh Nauk **183** (1) 3 – 32 (2013)
DOI: 10.3367/UFNr.0183.201301a.0003
Translated by the author; edited by A M Semikhatov

"If only you knew what trash gives rise
To verses that are not ashamed uprise..."
Anna Akhmatova

1. Introduction

Hadron interactions are strong and, in principle, should be described by quantum chromodynamics (QCD). However, experimental data show that their main features originate from the nonperturbative sector of QCD. Only comparatively rare processes with large transferred momenta can be treated theoretically rather successfully by perturbative methods due to the well-known property of the asymptotic freedom of QCD. Hence, in the absence of methods for a rigorous solution of QCD equations, our understanding of the dynamics of the main bulk of strong interactions is severely limited by model building or some rare rigorous relations. In fact, our approach to high-energy hadronic processes at present is at best still in its infancy.

As has been learned from experiment, strong interactions of colliding high-energy particles give rise to inelastic and elastic processes. Some new particles (mostly pions) are produced in inelastic processes, which are the most probable ones, comprising 75% to 80% of all processes at high energies. Most created particles have comparatively small transverse momenta.

At the same time, in 25% to 20% of events, the colliding particles do not change their nature and scatter elastically, declining at some angle from their initial trajectories. The only information about this process available from experiment is obtained by the measurement of the differential cross section (proportional to the probability) of elastic scattering at some angle at a given energy.

In a very tiny range of extremely small angles, the charged particles scatter due to electromagnetic forces. But the dominant process of elastic scattering due to strong interactions proceeds at somewhat larger angles in the so-called diffraction cone. The differential cross sections are heavily weighted toward small transferred momenta exhibiting a huge peak. The scattering angle is still rather small there and becomes smaller and smaller as the energy increases. The probability of scattering at a given angle in this region

decreases steeply, similarly to a Gaussian exponential. Noticeably less than one percent of particles are elastically scattered to larger angles outside this diffraction cone. The Gaussian behavior is replaced there by a simple exponential one with some shoulders and (or) dips. At ever larger angles (or transferred momenta), a power-like decrease has been observed. At angles close to $\pi/2$, some additional flattening is seen.

The elastic cross section (the integral of the differential distribution over angles or transverse momentum) depends on the energy of the colliding partners. At high energies, it shows a steady tendency to become larger with an increase in energy. We note that the inelastic cross section also increases, such that their sum (the total cross section) increases as well.

The process of elastic scattering of hadrons has been studied experimentally in a wide energy range with different initial particles. At high energies of colliding partners, the most detailed results are available for the scattering of protons (pp) and antiprotons ($p\bar{p}$) on protons. We mainly discuss these data, sometimes referring to other colliding partners of protons such as pions and kaons.

Some surprises in the behavior of differential cross sections appeared in the 1960s when the very first experimental data on elastic pp and πp scattering were obtained at energies between 6.8 and 19.2 GeV in laboratory system [1–11] (the total energy in the center-of-mass system (cms) is only $\sqrt{s} \approx 4-6$ GeV!). The diffraction cone behavior changed at larger transferred momenta $|t|$ to a slower t-dependence. Somewhat later, the energy range was extended to 50 GeV [12–14]. With the advent of new accelerators, the data for pp scattering at energies $\sqrt{s} \approx 19$, 20, 23, 28, 31, 45, 53, 62 GeV were published [15–30], and the data for $p\bar{p}$ at 31, 53, 62, 546, 630, 1800, 1980 GeV [31–44] appeared. The early results are reviewed in Refs [45, 46]. The compilation of the data can be found in [47]. Only recently, the results of the TOTEM collaboration at the LHC on elastic pp scattering processes at $\sqrt{s} = 7$ TeV were published [48, 49].

Surely, these results called for their understanding and theoretical interpretation. The most important task is to acquire some knowledge about the internal structure of colliding particles by deciphering the information supplied by experimental data about the dependence on energy and transferred momentum. The transferred momentum is directly related to the size and the structure of those regions inside the hadron that participate in the interaction.

Many phenomenological models have been proposed. Most of them aspire to be a 'phenomenology of everything' related to elastic scattering of hadrons in a wide energy range. Doing so in the absence of applicable laws and methods of the fundamental theory, they have to use a large number of adjustable parameters. The free parameters have been determined by fitting the model results to the available experimental data. Even then, model predictions often fail when a new energy domain becomes accessible. And the 'verse' does not grow anymore! (If not recultivated.) Independent of their success and failure, we are sure that "in the long run, the physical picture may be expected to be much more important than most of the detailed computations" [50]. In what follows, we mention and discuss many of them.

The scattering of charged particles at extremely small angles is completely dominated by the Coulomb amplitude. The absolute value of the Born amplitude is well known. The phase of the Coulomb amplitude varies depending on the model chosen. However, this variation is rather mild in the considered tiny region of extremely small angles. The interference of the Coulomb amplitude with the strong-interaction (nuclear) amplitude in the transition region where they are almost equal has been used for the experimental determination of the ratio of the real to imaginary parts of the nuclear amplitude. This interference also depends on the chosen form of the nuclear amplitude. Theoretically, this ratio can be estimated with the help of dispersion relations. We briefly discuss this problem and show how the obtained results influence our analysis of scattering at somewhat larger angles.

The most numerous group of models deals with phenomenological attempts to describe the main bulk of elastic scattering at small angles in the diffraction cone. In general, they are based on some geometric models of particle substructure, with peripheral regions playing the decisive role. The approach using Reggeon (Pomeron) exchanges is the most popular among them. The approximately Gaussian (in angles) shape of the experimentally measured differential cross section in this region has been fitted just in this way. In addition to it, the simplest classical expressions for diffractive processes and results on the electromagnetic form factors are also used. However, the bold extension of the obtained results to larger angles is usually not very successful, even if some new parameters are introduced.

Particles scattered at larger angles give insight into the deeper internal regions of particle structure. The multiple iteration (rescattering) of diffractive processes can explain the region of angles that are somewhat larger than the diffractive ones. Without any additional model building, it can be described as a consequence of the unitarity condition. The only necessary input is the experimentally known energy behavior of the diffraction cone slope and the total cross section. This allows predicting the observed exponential fall-off with angles and damped oscillations imposed on it, which, depending on their amplitudes, lead to shoulders or dips of the differential cross sections.

At somewhat larger angles, the elastic processes can be considered to be dominated by the innermost constituents of the colliding particles. The perturbative QCD approach to hard parton scattering convoluted with some results or the parton structure of colliding particles is then used to describe experimental data. This approach predicts a power-like angular dependence of the differential cross sections. It has been seen in experiment. The dimensional (or quark) counting of the number of participating partons has been successful. The convolution with the internal structure of particles implies some coherence in the behavior of its constituents: all of them should coherently turn at the same angle. A particle should not be destroyed during the collision, and its internal wave function must be left intact. Therefore, we can call such processes coherent large-angle scattering.

At angles close to $\pi/2$, the effects of symmetrization of the corresponding amplitudes can become important and lead to some flattening of the differential distribution.

There are no strict definitions of the lower and upper bounds of these regions. The diffraction peak shrinks with energy, such that the exponential fall-off with the squared transferred momenta t terminates at ever smaller values. Correspondingly, the dip after it shifts to smaller values of $|t|$, as does the $\sqrt{|t|}$-exponential. At low energies, this regime approximately occupies the interval between 0.8 and 2 GeV^2, while in the LHC, it has moved to 0.4–1.5 GeV^2. According to the QCD prejudice, the scale for parton scattering should be

set above 1 GeV^2. This is actually observed with a power-like decrease starting somewhere around $|t| > 1.5-2$ GeV^2 at the LHC.

Hence, we can speak, at least, about five subregions of elastic scattering. We mainly discuss three of them: the diffraction cone, the Orear regime, and coherent hard parton scattering. The diffraction cone is well known to us from semiclassical effects. The regions beyond it became noticeable only at energies of colliding particles above several GeV, where processes of scattering at sufficiently large angles or transferred momenta are observable. They persist up to the present LHC energy of 7 TeV. Who ordered them and whether they will survive at ever higher energies are also questions to be discussed in this review.

The structure of this paper is as follows. The main relations between different characteristics of elastic scattering are presented in Section 2. Then, in Section 3, their global dependences on energy and transferred momenta are discussed, together with our attempts to understand their implications within the simplest approaches. A more detailed analysis of experimental data in the framework of different theoretical ideas and approximations is the content of Section 4. Finally, the general picture is briefly discussed in Section 5.

We do not consider the scattering of polarized particles, and the spin structure of the amplitude is ignored.

2. Main relations

As discussed above, the measurement of the differential cross section is the only source of experimental information about a process. Hence, the main characteristics of hadron interactions directly related to the elastic scattering amplitude, such as the total cross section, the elastic scattering cross section, the ratio of the real to the imaginary part of the amplitude, and the slope of the diffraction cone, are obtained. The first two are functions of the total energy only, while the others depend on two variables: the total energy and the transferred momentum (or the scattering angle).

The dimensionless elastic scattering amplitude A defines the differential cross section as

$$\frac{\mathrm{d}\sigma(s)}{\mathrm{d}t} = \frac{1}{16\pi s^2}|A|^2 = \frac{1}{16\pi s^2}\left(\operatorname{Im} A(s,t)\right)^2\left(1+\rho^2(s,t)\right), \quad (1)$$

where the ratio of the real to imaginary parts of the amplitude is defined:

$$\rho(s,t) = \frac{\operatorname{Re} A(s,t)}{\operatorname{Im} A(s,t)}. \quad (2)$$

In what follows, we consider very high energy processes. Therefore, the masses of the colliding particles can be neglected, and we use the expression $s = 4E^2 \approx 4p^2$, where E and p are the energy and momentum in the center-of-mass system. The four-momentum transfer squared is

$$-t = 2p^2(1-\cos\theta) \approx p^2\theta^2 \approx p_\mathrm{t}^2, \quad \theta \ll 1, \quad (3)$$

with θ denoting the scattering angle in the center-of-mass system and p_t being the transverse momentum.

The elastic scattering cross section is given by the integral of differential cross section (1) over all transferred momenta:

$$\sigma_\mathrm{el}(s) = \int_{t_\mathrm{min}}^{0} \mathrm{d}t\, \frac{\mathrm{d}\sigma(s)}{\mathrm{d}t}. \quad (4)$$

The total cross section σ_t is related by the optical theorem to the imaginary part of the forward scattering amplitude as

$$\sigma_\mathrm{t}(s) = \frac{\operatorname{Im} A(p,\theta=0)}{s}. \quad (5)$$

Elastically scattered hadrons escape from the interaction region declining mostly at quite small angles within the so-called diffraction cone.[1] Therefore, the main focus has been on this region. As is known from experiment, the diffraction peak has a Gaussian shape in the scattering angles or decreases exponentially as a function of the transferred momentum squared:

$$\frac{\mathrm{d}\sigma/\mathrm{d}t}{(\mathrm{d}\sigma/\mathrm{d}t)_{t=0}} = \exp(Bt) \approx \exp(-Bp^2\theta^2). \quad (6)$$

In view of relations (4)–(6), any successful theoretical description of the differential distribution must also work in fitting the energy dependences of the total and elastic cross sections. The diffraction cone slope B is given by

$$B(s,t) \approx \frac{\mathrm{d}}{\mathrm{d}t}\left(\ln\frac{\mathrm{d}\sigma(s,t)}{\mathrm{d}t}\right). \quad (7)$$

Actually, the slope B depends slightly on t at a given energy s, e.g., at the LHC, its value changes by about 10% within the cone for $|\Delta t| \approx 0.3$ GeV^2. We neglect this in the first approximation. The normalization factor in Eqn (6) is

$$\left(\frac{\mathrm{d}\sigma}{\mathrm{d}t}\right)_{t=0} = \frac{\sigma_\mathrm{t}^2(s)\left(1+\rho_0^2(s)\right)}{16\pi}, \quad (8)$$

where ρ_0 is defined as the ratio of the real and imaginary parts of the amplitude in the forward direction at $\theta = t = 0$. Equation (8) follows from formula (1) and optical theorem (5) at $t = 0$.

According to the dispersion relations, which connect the real and imaginary parts of the amplitude, and optical theorem (5), the value ρ_0 can be expressed as an integral of the total cross section over the whole energy range. In practice, ρ_0 is mainly sensitive to the local derivative of the total cross section. In the first approximation, the result of the dispersion relation can then be written in the form [51–54]

$$\rho_0(s) \approx \frac{1}{\sigma_\mathrm{t}}\left[\tan\left(\frac{\pi}{2}\frac{\mathrm{d}}{\mathrm{d}\ln s}\right)\right]\sigma_\mathrm{t} = \frac{1}{\sigma_\mathrm{t}}\left[\frac{\pi}{2}\frac{\mathrm{d}}{\mathrm{d}\ln s} + \frac{1}{3}\left(\frac{\pi}{2}\right)^3\frac{\mathrm{d}^3}{\mathrm{d}\ln s^3} + \ldots\right]\sigma_\mathrm{t}. \quad (9)$$

It follows that at high energies, $\rho_0(s)$ is mainly determined by the derivative of the logarithm of the total cross section with respect to the logarithm of energy.

The bold extension of the first term in this series to nonzero transferred momenta would look like

$$\rho(s,t) \approx \frac{\pi}{2}\left(\frac{\mathrm{d}\ln\operatorname{Im} A(s,t)}{\mathrm{d}\ln s} - 1\right). \quad (10)$$

[1] In practice, the tiny region of the interference of the Coulomb and nuclear amplitudes at extremely small angles does not contribute to the total cross section of elastic scattering. Its role in obtaining some estimates of $\rho(s,t)$ is described below.

If we neglect the high-$|t|$ tail of the differential cross section, which is several orders of magnitude lower than the optical point, and integrate in Eqn (4) using expression (6) with constant B, we obtain the approximate relation between the total cross section, the elastic cross section, and the slope:

$$\frac{\sigma_{\rm t}^2(1+\rho_0^2)}{16\pi B\sigma_{\rm el}} \approx 1\,. \tag{11}$$

We can compare this formula with the upper bound obtained in Ref. [55]:

$$\frac{\sigma_{\rm t}^2}{18\pi B\sigma_{\rm el}} \leqslant 1\,. \tag{12}$$

The phase ζ of the hadronic amplitude is often defined as

$$A(s,t) = {\rm i}\big|A(s,t)\big| \exp\big[-{\rm i}\zeta(s,t)\big]\,; \tag{13}$$

then

$$\rho(s,t) = \tan\zeta(s,t)\,. \tag{14}$$

These formulas are used for measuring the luminosity, which relates the cross section σ_i of a given process i to the corresponding number of events N_i by

$$L = \frac{N_i}{\sigma_i}\,. \tag{15}$$

A simultaneous measurement of the total number of events $N_{\rm t}$ and the number of elastic events $N_{\rm el}$ is used to define the luminosity as

$$L = \frac{1+\rho_0^2}{16\pi}\,\frac{N_{\rm t}^2}{{\rm d}N_{\rm el}/{\rm d}t\big|_{t=0}}\,. \tag{16}$$

The measured total cross section is independent of luminosity:

$$\sigma_{\rm t} = \frac{16\pi}{1+\rho_0^2}\,\frac{{\rm d}N_{\rm el}/{\rm d}t\big|_{t=0}}{N_{\rm t}}\,. \tag{17}$$

The elastic scattering amplitude must satisfy the general properties of analyticity, crossing symmetry, and unitarity. The unitarity of the S-matrix, $SS^+ = 1$, imposes certain requirements on it. In the s-channel, we have

$$\begin{aligned}
&{\rm Im}\,A(p,\theta) = I_2(p,\theta) + F(p,\theta)\\
&= \frac{1}{32\pi^2}\int\int {\rm d}\theta_1\,{\rm d}\theta_2\,\sin\theta_1\sin\theta_2 A(p,\theta_1)A^*(p,\theta_2)\\
&\times\Big\{\big[\cos\theta - \cos(\theta_1+\theta_2)\big]\big[\cos(\theta_1-\theta_2)-\cos\theta\big]\Big\}^{-1/2} + F(p,\theta)\,.
\end{aligned} \tag{18}$$

The region of integration in (18) is defined by the conditions

$$|\theta_1-\theta_2| \leqslant \theta\,, \qquad \theta \leqslant \theta_1+\theta_2 \leqslant 2\pi-\theta\,. \tag{19}$$

The integral term represents the two-particle intermediate states of the incoming particles. The function $F(p,\theta)$ represents the shadowing contribution of the inelastic processes to the elastic scattering amplitude. Following [56], we call it the overlap function. It determines the shape of the diffraction peak and is completely nonperturbative. Only some phenomenological models can claim to describe it.

In the forward direction $\theta = 0$, this relation, in combination with optical theorem (5), reduces to the general statement that the total cross section is the sum of cross sections of elastic and inelastic processes:

$$\sigma_{\rm t} = \sigma_{\rm el} + \sigma_{\rm in}\,. \tag{20}$$

Unitarity relation (18) has been successfully used [57–60] for the model-independent description of the Orear region between the diffraction cone and hard parton scattering, which became the crucial test for phenomenological models.

Experimentally, all characteristics of elastic scattering are measured as functions of the energy s and transferred momentum t. However, it is desirable to have concrete information on the geometric structure of scattered particles and the role of different spatial regions in the scattering process. We should use the Fourier–Bessel transform to obtain the correspondence between the transferred momenta and these space regions. The transverse distance between the centers of colliding particles, called the impact parameter $\mathbf{b}$, determines the effective transferred momentum t. The amplitudes in the corresponding representations are related as

$$h(s,b) = \frac{1}{16\pi s}\int_{t_{\rm min}=-s}^{0} {\rm d}t\,A(s,t)\,J_0(b\sqrt{-t}\,)\,. \tag{21}$$

More peripheral collisions with large b lead to smaller transferred momenta $|t|$.

The amplitude $A(s,t)$ can be connected to the eikonal phase $\delta(s,\mathbf{b})$ and to the opaqueness (or blackness) $\Omega(s,\mathbf{b})$ at the impact parameter $\mathbf{b}$ by the Fourier–Bessel transformation

$$\begin{aligned}
A(s,t=-q^2) &= \frac{2s}{\rm i}\int {\rm d}^2b\,\exp({\rm i}\mathbf{qb})\big[\exp\big(2{\rm i}\delta(s,\mathbf{b})\big)-1\big]\\
&= 2{\rm i}s\int {\rm d}^2b\,\exp\big({\rm i}\mathbf{qb}\big)\big[1-\exp\big(-\Omega(s,\mathbf{b})\big)\big]\,.
\end{aligned} \tag{22}$$

The integration is over the two-dimensional space of the impact parameter $\mathbf{b}$.

Assuming $\Omega(s,\mathbf{b})$ to be real and using Eqn (5), we obtain

$$\sigma_{\rm t} = 4\pi\int_0^\infty \big[1-\exp\big(-\Omega(s,\mathbf{b})\big)\big]\,b\,{\rm d}b\,. \tag{23}$$

Also,

$$\sigma_{\rm el} = 2\pi\int_0^\infty \big[1-\exp\big(-\Omega(s,\mathbf{b})\big)\big]^2 b\,{\rm d}b\,, \tag{24}$$

$$B = \frac{\int_0^\infty \big[1-\exp\big(-\Omega(s,\mathbf{b})\big)\big]b^3\,{\rm d}b}{2\int_0^\infty \big[1-\exp\big(-\Omega(s,\mathbf{b})\big)\big]b\,{\rm d}b}\,. \tag{25}$$

To apply the inverse transformation, we must know the amplitude $A(s,t)$ at all transferred momenta. Therefore, it is necessary to continue it analytically to the nonphysical region of t [61, 62]. This can be done [63]. Correspondingly, the mathematically consistent inverse formulas generally contain the sum of contributions from the physical and nonphysical parts of the amplitude $A(s,t)$. Unitarity condition (18) involves only the amplitude in the physical region; only this part of its Fourier–Bessel transform is important in the unitarity relation for the impact parameter representation. It is written as

$${\rm Im}\,h(s,b) = \big|h(s,b)\big|^2 + F(s,b)\,, \tag{26}$$

where $h(s,b)$ and $F(s,b)$ are obtained by the direct transformation of $A(s,t)$ and $F(s,t)$ integrated only over the physical transferred momenta from $t_{\min}$ to 0. They show the dependence of the intensity of elastic and inelastic interactions on the mutual impact parameter of the colliding particles. Analogously to relation (20), the integrals over all impact parameter values in this relation respectively represent the total, elastic, and inelastic cross sections. It is especially simple to calculate the overlap function from algebraic equation (26) if the real part is small in some subregion, i.e., $|h(s,b)| \approx \operatorname{Im} h(s,b)$. Then

$$\operatorname{Im} h(s,b) \approx \frac{1}{2}\left(1 - \sqrt{1 - 4F(s,b)}\,\right). \tag{27}$$

In the region where the transformed overlap function is small, $F(s,b) \ll 1$, the imaginary part is also small: $\operatorname{Im} h(s,b) \approx F(s,b)$.

However, the accuracy of the unitarity condition in b-representation (26) is still under discussion [61–65], because some corrections due to the nonphysical region enter there, even though their role may be negligible. Moreover, the further use of the approximate formulas of the quasi-eikonal unitarization often leads to failure in describing the differential cross section outside the diffraction cone.

The average values of the impact parameters for all — elastic and inelastic — processes can be estimated from the amplitude $A(s,t)$ if we assume that $\mathrm{d}\rho/\mathrm{d}t = 0$ at $t = 0$ [64]:

$$\left\langle b^2(s)\right\rangle_{\text{tot}} = \frac{\sigma_{\text{el}}}{\sigma_{\text{t}}}\left\langle b^2(s)\right\rangle_{\text{el}} + \frac{\sigma_{\text{in}}}{\sigma_{\text{t}}}\left\langle b^2(s)\right\rangle_{\text{in}} = 2B(s,0)\,, \tag{28}$$

where, e.g.,

$$\left\langle b^2(s)\right\rangle_{\text{el}} = 4\int_{t_{\min}}^{0} \mathrm{d}t\,|t|\left|\frac{\mathrm{d}}{\mathrm{d}t}\,A(s,t)\right|^2 \left(\int_{t_{\min}}^{0} \mathrm{d}t\,\left|A(s,t)\right|^2\right)^{-1}. \tag{29}$$

Nevertheless, the problem of the relative contributions of the central (small b) and peripheral (large b) regions under elastic hadron collisions is still widely disputed. We must be especially careful when considering unitarity condition (26) with small impact parameters for certain models. Slight variations of $h(s,b)$ in this region may lead to strong variations of the amplitude $A(s,t)$ at large $|t|$.

The elastic scattering at extremely small angles allows estimating the forward ratio of the real part of the amplitude to its imaginary part ρ_0 in experiment. For completeness, we show an approximate expression for the amplitude $A(s,t)$ in the region dominated by the Coulomb amplitude and its interference with the nuclear amplitude:

$$A^{\text{CN}}(s,t) = \mp\frac{8\pi\alpha}{|t|}\,s f_1\big(|t|\big) f_2\big(|t|\big)\exp\left(\mathrm{i}\alpha\Phi\right) + \big(\mathrm{i} + \rho_0(s)\big)s\sigma_{\text{t}}\exp\frac{Bt}{2}\,, \tag{30}$$

where the upper (lower) sign corresponds to the scattering of particles with the same (opposite) electric charges, the form factors of two colliding particles $f_j(|t|)$ added 'by hand' in Eqn (30) take their internal composition into account, Φ is the Coulomb phase, and $\alpha = 1/137$ is the fine structure constant. The expressions for $f_j(|t|)$ and Φ depend on various prescriptions for them obtained with different assumptions concerning the internal structure of a hadron. The most popular shapes of the form factors are either the Gaussian fall-off with an increasing angle, like $\exp(2t/\Lambda^2)$, similar to that in (6), or the dipole (power-like) approximation, like $(1 - t/\Lambda^2)^{-2}$, with some more complicated subleading factors. The phase Φ usually contains a term with the typical logarithmic dependence on the angle θ, which becomes large at very small angles, and some subleading terms. In both cases, the subleading terms have to contain additional free parameters for a more accurate description of experimental data. As we see, the ratio $\rho(s,t)$ in (2) is approximated by $\rho(s,0) = \rho_0$ in the fit (30). This implies that both real and imaginary parts of the nuclear amplitude exhibit the same purely exponential t-dependence in the interference region (with the dominance of the imaginary part for small ρ_0). More details can be found in [66–81].

3. Where do we stand now?

We first discuss the asymptotic properties of fundamental characteristics such as the total cross section σ_{t}, the elastic cross section σ_{el}, the ratio of the real part to the imaginary part of the elastic amplitude ρ, and the width of the diffraction peak B at infinite energies. Then we compare this with some trends in present experimental data.

More than half a century ago, it was claimed in [82, 83] that according to the general principles of field theory and ideas about hadron interactions, the total cross section cannot increase with energy faster than $\ln^2 s$. The upper bound was recently improved [84], with the coefficient in front of the logarithm shown to be half that in the earlier limit,

$$\sigma_{\text{t}} \leqslant \frac{\pi}{2m_\pi^2}\ln^2\frac{s}{s_0}\,, \tag{31}$$

where m_π is the pion mass. If estimated at present energies, this bound is still much higher than the experimentally measured values of the cross sections, with $s_0 = 1$ GeV^2 chosen as a 'natural' scale. Therefore, this is only a functional constraint; it forbids extremely fast growth of the total cross section, asymptotically exceeding the above limits. Both the coefficient in front of the logarithm in (31) and the constancy of s_0 are often questioned. In particular, some possible dependence of s_0 on the energy s has been pointed out (see, e.g., [85]).

The Heisenberg uncertainty relation shows that such a regime favors an exponentially bounded spatial profile of the matter density distribution $D(r)$ in colliding particles, such as $D(r) \propto \exp(-mr)$. Because the energy density is $ED(r)$ and there should be at least one created particle with mass m in the overlap region, the condition $ED(r) = m$ leads to $r \leqslant (1/m)\ln(s/m^2)$ and, consequently, to the functional dependence in (31).

It was Heisenberg who first proposed such a behavior of total cross sections [86]. He considered the pion production processes in proton–proton collisions as a shock wave problem governed by some nonlinear field theory equations.

To study the asymptotic regime, some theoretical arguments based on the general principles of field theory and the analogy of strong interactions to massive quantum electrodynamics [87] were promoted. The property that the limits as $s \to \infty$ and $M \to 0$ (where M is the photon mass) commute has been used [88], implying that the asymptotic domain of strong interactions coincides with the massless limit of quantum electrodynamics. These studies led to the general geometric picture of two hadrons colliding with asymptotically high energies and interacting as Lorentz-contracted

Table 1. The gray and Gaussian disks models ($X = \sigma_{el}/\sigma_t$, $Z = 4\pi B/\sigma_t$).

Model	$1 - \exp(-\Omega) = \Gamma(s,b)$	σ_t	B	X	Z	X/Z	XZ
Gray	$\alpha\theta(R-b),\ 0 \leqslant \alpha < 1$	$2\pi\alpha R^2$	$R^2/4$	$\alpha/2$	$1/2\alpha$	α^2	$1/4$
Gaussian	$\alpha \exp(-b^2/R^2),\ 0 \leqslant \alpha \leq 1$	$2\pi\alpha R^2$	$R^2/2$	$\alpha/4$	$1/\alpha$	$\alpha^2/4$	$1/4$

black disks (see also review paper [89]). In what follows, we discuss some other possibilities as well. But as a starting point for further reference, we describe the predictions of this proposal.

The main conclusions are:

(1) For black ($\Omega(s,\mathbf{b}) \to \infty$) and logarithmically expanding disks with finite radii R ($R = R_0 \ln s$, $R_0 = \text{const}$), it follows from (23) that σ_t asymptotically approaches infinity as

$$\sigma_t(s) = 2\pi R^2 + O(\ln s)\,, \quad R = R_0 \ln s\,, \quad R_0 = \text{const}\,. \tag{32}$$

(2) The elastic and inelastic processes make equal contributions to the total cross section:

$$\frac{\sigma_{el}(s)}{\sigma_t(s)} = \frac{\sigma_{in}(s)}{\sigma_t(s)} = \frac{1}{2} \mp O(\ln^{-1} s)\,. \tag{33}$$

This quantum mechanical result differs from 'intuitive' classical predictions.

(3) The width of the diffraction peak $B^{-1}(s)$ must shrink because its slope increases as (see also [90])

$$B(s) = \frac{R^2}{4} + O(\ln s)\,. \tag{34}$$

(4) The forward ratio of the real part to the imaginary part of the amplitude ρ_0 must vanish asymptotically as

$$\rho_0 = \frac{\pi}{\ln s} + O(\ln^{-2} s)\,. \tag{35}$$

This result follows directly from Eqn (9) for $\sigma_t \propto \ln^2 s$.

(5) The differential cross section has a shape resembling the classical diffraction of light on a disk:

$$\frac{d\sigma}{dt} = \pi R^4 \left(\frac{J_1(qR)}{qR}\right)^2, \tag{36}$$

where $q^2 = -t$.

(6) The product of σ_t with the value γ of $|t|$ at which the first dip in the differential elastic cross section occurs is a constant independent of the energy:

$$\gamma\sigma_t = 2\pi^3\beta_1^2 + O(\ln^{-1} s) = 35.92 \text{ mb GeV}^2\,, \tag{37}$$

where $\beta_1 = 1.2197$ is the first zero of $J_1(\beta\pi)$.

These are merely a few conclusions among many others, albeit model-dependent ones.

None of these asymptotic predictions have been observed yet in experiment.

Surely, there is another possibility — more realistic at present energies — that the black disk model is too extreme and the gray fringe always exists. It opens the way to much speculation, with many new parameters concerning particle shape and opacity (see, e.g., [78, 80, 81, 91–102]).

The black disk limit might be unrealistic. Therefore, in Table 1 we show the predictions of the gray disk model with the steep rigid edge described by the Heaviside step-function and the Gaussian disk model. The total cross section, the slope B, the ratio of the elastic to total cross section $X = \sigma_{el}/\sigma_t$, the ratios $Z = 4\pi B/\sigma_t$ and X/Z, and the product XZ are displayed there; $\Gamma(s,b)$ is the diffraction profile function.

The slope B is completely determined by the size of the interaction region R. Other characteristics are sensitive to the blackness of disks α. In particular, the ratio X is proportional to α. The ratio Z plays an important role for fits at larger angles, as explained in Section 4.2. It is inversely proportional to α. The corresponding formulas are given by (23)–(25). The black-disk limit follows from the gray-disk model at $\alpha = 1$. For a Gaussian distribution of matter, the disk becomes nontransparent at its center in this limit. The parameter XZ is constant in these models and does not depend on the nucleon transparency. On the contrary, the parameter X/Z is very sensitive to it, being proportional to α^2. Therefore, it would be extremely instructive to obtain knowledge about them from experimental data.

In Table 2, we show how the above ratios evolve with energy according to experimental data. Most of the entries, except the last two, are taken from Refs [91, 103], with the simple recalculation $Z = 1/4Y$. The data at Tevatron and LHC energies are taken from Refs [48, 49, 104]. All results are for pp scattering, except those at 546 and 1800 GeV for $p\bar{p}$ processes, which should be close to pp at these energies. The accuracy of the numbers listed in Table 2 can be very approximately estimated to be better than $\pm 10\%$ from known error bars for the cross sections and the slopes.

Table 2. The energy behavior of various characteristics of elastic scattering.

$\sqrt{s}$, ГэВ	2.70	4.11	4.74	6.27	7.62	13.8	62.5	546	1800	7000
X	0.42	0.28	0.27	0.24	0.22	0.18	0.17	0.21	0.23	0.25
Z	0.64	1.02	1.09	1.26	1.34	1.45	1.50	1.20	1.08	1.00
X/Z	0.66	0.27	0.25	0.21	0.17	0.16	0.11	0.18	0.21	0.25
XZ	0.27	0.28	0.29	0.30	0.30	0.26	0.25	0.26	0.25	0.25

The most interesting feature of the experimental results is the minimum of the blackness parameter α at ISR energies. It can be clearly seen in the minima of X and X/Z and in the maximum of Z at $\sqrt{s} = 62.5$ GeV. The steady decrease in ratios X proportional to α and X/Z proportional to α^2 up to the ISR energies and their increase at Sp$\bar{p}$S, Tevatron, and LHC energies means that the nucleons become more transparent up to the ISR energies and more black toward 7 TeV. The same conclusion follows from the behavior of Z, which is inversely proportional to α. The value of Z rapidly approaches its limit for the Gaussian distribution of matter in the disk. For the Gaussian shape, the parameter X/Z cannot exceed 0.25. This model is excluded only at low energies. According to Eqn (12), $XZ \approx 0.25(1 + \rho_0^2)$, which is indeed close to 0.25 within the experimental errors, the estimate of $\rho_0^2 \leqslant 0.02$, and slight variations of B inside the cone in the framework of our crude model as predicted in Table 1. This

shows that our models are not bad for qualitative estimates in a first approximation.

Before discussing various fits, we briefly comment on some important general trends in high-energy data observed in experiment.

(1) Total cross sections increase with energy. At present energies, the power-like approximation is the most preferable one. The preasymptotic behavior of σ_t proposed in earlier papers [87, 88] was

$$\sigma_t \propto s^a \ln^{-2} s\,, \tag{38}$$

where the numerical value of a was estimated to be of the order of unity in strong interactions. It was shown in [105] to lie in the range between 0.08 and 0.2, which is close to values obtained in recent phenomenological fits. The power-law increase persists in a wide interval of energies (see Ref. [106] for the recent analysis of experimental data). Consequently, the density distribution in colliding particles is closer to a power-like dependence than to an exponential one in that energy range.

(2) The ratio $X = \sigma_{el}/\sigma_t$ decreases from low energies to those of ISR, where it becomes approximately 0.17 and then strongly increases to 0.25 at the LHC energies. However, it is still quite far from the asymptotic value 0.5, corresponding to the black-disk limit.

The only higher-energy data came from the Pierre Auger collaboration, which recently reported [107] a measurement of the inelastic p–air cross section σ_{in}^{p-air} at $\sqrt{s} = 57 \pm 6$ TeV. After some corrections and Glauber model calculations, it results in the pp inelastic cross section $\sigma_{in}^{pp} \approx 90$ mb. Some models [108–110] extrapolate their predictions for the total cross section to this energy and obtain a value of about 135 mb. Hence, the ratio of the inelastic to the total cross section could become equal to 0.67, which is smaller than 0.75 at 7 TeV. However, it is premature to reach any definite conclusions because of large errors in the cosmic ray data and the underestimated value of the total cross section predicted to be 7 TeV by the model [108–110]. The extrapolation to infinite energies done in the same model leads to this ratio estimated as 0.509, which is compatible with the black-disk predictions. Still, asymptopia is but an elusive concept!

Sometimes, the modified black-disk limit is attributed to the sum of elastic and diffractive processes [111]. It may then be that

$$\frac{\sigma_{el} + \sigma_{diff}}{\sigma_t} \to \frac{1}{2}\,, \tag{39}$$

where σ_{diff} is the sum of cross sections of single and double inelastic diffraction. The fits in Ref. [106] suggest that the relations

$$\frac{\sigma_{el}}{\sigma_t} \to \frac{1}{3}\,, \qquad \frac{\sigma_{diff}}{\sigma_t} \to \frac{1}{6} \tag{40}$$

can be valid separately.

(3) The diffraction peak shrinks about twice from energies $\sqrt{s} \approx 6$ GeV, where $B \approx 10$ GeV^{-2}, to the LHC energy, where $B \approx 20$ GeV^{-2}. At the ISR energies, the slope $B(s)$ increases logarithmically. Accounting for LHC data requires a stronger dependence than a simple logarithmic one. The terms proportional to $\ln^2 s$ are usually added in phenomenological fits. Even then, predictions [112, 113] are not completely satisfactory. At present energies, in connection with the power-like preasymptotic behavior of σ_t, we could also expect a faster-than-logarithmic shrinkage of the diffraction peak.

The tendency in the peak behavior at larger $|t|$ also changes with an energy increase. In the energy region up to ISR, it becomes less steep near its end (see Figs 4 and 5 in Ref. [45]), but its slope increases at the LHC energies. Both the minimum and maximum following the peak shift to smaller $|t|$.

As regards the behavior of the differential cross section as a function of the transverse momentum behind the maximum, the t-exponential of the diffraction peak is replaced, according to experimental data, by a $(-\sqrt{|t|} \approx -p_t)$-exponential at the intermediate angles:

$$\frac{d\sigma}{dt} \propto \exp\left(-2a\sqrt{|t|}\right), \qquad a \approx \sqrt{B}\,. \tag{41}$$

The slope $2a$ in this region also increases with the energy, and the whole Orear region shifts to the ever lower transferred momenta.

In this connection, we also note an intriguing property of the ratio $Z = 4\pi B/\sigma_t$, which is closely related to the value of the slope B. From Table 2, we see that it is about 1 at $\sqrt{s} = 4$ GeV, increases to 1.5 at ISR energies, and then again drops to around 1 at 7 TeV. This ratio, in combination with values of ρ at different angles, determines the slope in the $|t|$ region beyond the diffraction peak at any s (see Ref. [58] and the discussion in Section 4.2.2). According to Eqns (32) and (34), Z should decrease and be asymptotically equal to $1/2$ in the black-disk limit, such that the relation

$$\sigma_t = 8\pi B \tag{42}$$

be asymptotically fulfilled. At the LHC energy 7 TeV, the coefficient in the right-hand side is still half as much. However, if the preasymptotic power-like increase in the total cross section accompanied by a slower increase in the slope persists, the tendency to this limit looks quite promising.

The relation between σ_t and B is also discussed in Refs [106, 114]. In particular, the fits in [106] correspond to the value $Z \approx 0.93$ at Auger energies 57 ± 6 TeV, i.e., lower than 1 at 7 TeV.

(4) As a function of energy, the ratio ρ_0 increases from negative values at comparatively low energies, crosses zero in the region of hundreds of GeV, and becomes positive at higher energies. This is a general tendency for collisions of any initial particles. For pp scattering, the prediction of (35) with values of s scaled by 1 GeV is still somewhat higher (about 0.177) than the estimates from dispersion relations (≈ 0.14 in Refs [110, 115]), even at 7 TeV, while strongly overshooting them at ISR, where $\pi/\ln s \approx 0.37$. No logarithmic decrease is seen in these predictions, which, however, depend on the behavior of the total cross section at higher energies. Moreover, the value 0.14 can only be reached according to (35) at the energy of 75 TeV. Probably, at energies higher than 75 TeV, the first signs of approach to the asymptotic regime will become visible. No data about ρ_0 at the LHC energies exist yet. The local value of ρ_0 estimated from Eqn (9) with a power-like fit of the total cross section, proportional to s^{Δ}, is $\rho_0 \approx \pi\Delta/2$. That agrees quite well with the soft Pomeron intercept $\Delta \approx 0.08$.

(5) To describe the shape of the differential cross section in the diffraction cone, significant corrections to Eqn (36) must be added at present energies. This is discussed in Section 4.1.

(6) The product $\gamma\sigma_{\rm t}$ changes from 39.5 mb GeV^2 at $\sqrt{s} = 6.2$ GeV to 51.9 mb GeV^2 at $\sqrt{s} = 7$ TeV and strongly deviates from the predicted asymptotic value (37). The total cross section $\sigma_{\rm t}$ increases faster than γ decreases.

From the geometrical standpoint, the general picture is one of protons becoming blacker, edgier, and larger (BEL) [116]. We conclude that even though the qualitative trends may be considered rather satisfactory, we are still quite far from the asymptotic regime, even at the LHC energies. This feature may be connected [117, 118] with the strong evolution of the parton content of strong interactions at present energies, revealing itself in an increase in the number of active parton pairs inside each proton with energy increase (higher density) and a softening of the structure functions, which leads to lower energy shares x for each parton pair (larger radii).

4. Experimental data and phenomenological models

As always, our knowledge about particular physical processes is limited by the practical possibility of measuring their characteristics. As mentioned above, numerous experimental data on elastic scattering of hadrons at various angles and at different energies have been obtained. Unfortunately, in some of them, the available region of angles is strongly limited by the experimental setup. Therefore, a comparison with theoretical proposals is possible only in the corresponding range of angles and energies.

The data and their fits at various energies and in different intervals of transferred momenta for different participating particles are so numerous that it is impossible to show all of them in a single review paper. Therefore, from the very beginning, we use the latest results of the TOTEM collaboration at the highest LHC energy, 7 TeV, as a reference point [48, 49]. The discussion of theoretical models is also concentrated around these data.

The total and elastic cross sections at 7 TeV are respectively estimated as 98.3 mb and 24.8 mb.[2] The figures from published papers [48, 49] demonstrating the behavior of the differential cross section as a function of the transferred momentum are displayed below. They clearly confirm the existence of the three regions discussed above.

The cross section shape in the region of the diffraction cone [48] is shown in Fig. 1. The t-exponential behavior with $B \approx 20.1$ GeV^{-2} is clearly seen at $|t| < 0.3$ GeV^2. The peak steepens at the end of the diffraction cone, and its slope becomes approximately 23.6 GeV^{-2} in the $|t|$ interval (0.36–0.47) GeV^2. The results at somewhat larger angles [49] in the Orear region are presented in Fig. 2. The dip at $|t| \approx 0.53$ GeV^2 with a subsequent maximum at $|t| \approx 0.7$ GeV^2 and the $\sqrt{|t|}$-exponential behavior are demonstrated. Some curves corresponding to different model predictions are also drawn here. The same data as in Fig. 2 are shown in Fig. 3, but with more details, including the steepened slope, the dip position, and the region of $|t|^{-8}$-behavior. The last one is ascribed to the hard parton scattering processes.

We congratulate all members of the TOTEM collaboration with this fantastic achievement! Their efforts are truly appreciated when estimating the values of angles at which the measurements had to be done. They were even smaller

[2] Here, we do not reproduce the statistical and systematic errors. They are shown in the original papers.

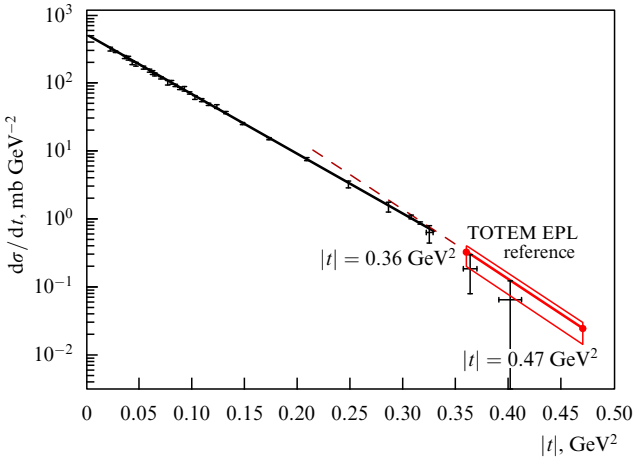

Figure 1. The differential cross section of elastic proton–proton scattering at $\sqrt{s} = 7$ TeV measured by the TOTEM collaboration (Fig. 4 in [49]). The region of the diffraction cone with the $|t|$-exponential decrease is shown.

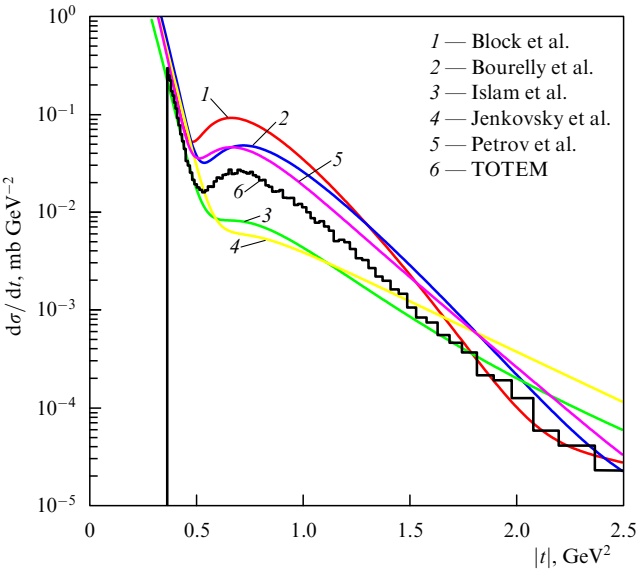

Figure 2. The differential cross section of elastic proton–proton scattering at $\sqrt{s} = 7$ TeV measured by the TOTEM collaboration (Fig. 4 in [48]). The region beyond the diffraction peak is shown. Predictions of five models are demonstrated.

than 10^{-4}! Detectors had to be installed at very long distances from the collision point to obtain results at low transferred momenta. These data revived interest in elastic scattering.

Theoretical models usually describe the diffraction cone and values of the total and elastic cross sections related to it more or less precisely (therefore, their fits are almost indistinguishable in that region and are not drawn in Fig. 1). However, all of them fail to quantitatively predict the behavior of the differential cross section outside the diffraction cone, as can be seen in Fig. 2. The predictions of five models [79, 92, 110, 119, 120] are drawn here. They are very widely spread around the experimental line. We can conclude that just this region becomes the Occam razor for all models. In what follows, we consider these models, as well as some others, in more detail.

The three intervals of $|t|$ (the diffraction cone, the Orear regime, and the region of hard parton scattering) are

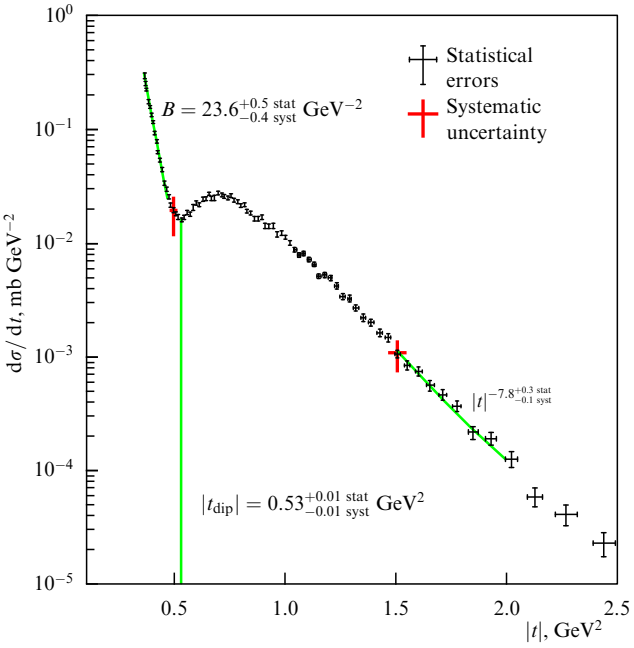

Figure 3. The differential cross section of elastic proton–proton scattering at $\sqrt{s} = 7$ TeV measured by the TOTEM collaboration (Fig. 3 in [48]). The same regions as in Fig. 2 are shown with the values of the steepened slope near the diffraction peak, the position of the dip, and the power-like behavior at the largest transferred momenta.

characterized by different dynamical content, as we understand it now. They require separate approaches to their descriptions. It seems reasonable that these regions are governed by different but interrelated physical mechanisms. In particular, different spatial regions of overlapping colliding objects are responsible for corresponding effects. Sections 4.1–4.3 are devoted to theoretical approaches to their explanation.

4.1 Diffraction cone and geometric approach

The internal structure of colliding, strongly interacting particles plays a crucial role in the outcome of their collisions. In high-energy hadron–hadron scattering, each hadron behaves as an extended object. They can be described by their size and the density of their constituents. The simplest models are demonstrated in Table 1.

Since long ago, it has been believed that hadrons contain some denser core surrounded by a meson (pion) cloud at their periphery. This idea was a cornerstone of the one-pion exchange model, which was first proposed in Ref. [121] to describe particle production in peripheral interactions. It evolved into the well-known multiperipheral and (multi)Reggeon exchange models (see, e.g., [122–124] for early review papers). They are rather successful in describing many features of multiparticle production processes. The multiperipheral approach developed, for instance, in the framework of the Bethe–Salpeter equation (see Ref. [124]) can be considered an attempt to account for the t-channel unitarity.

Nowadays, it is commonly believed that at very high energies, the total cross section is dominated by peripheral events. In modern parlance, this is related to the long-range nature of the field of 'perturbatively massless' gluons. The exchanged boson mass may mimic a nonperturbative mass gap in QCD with an 'effective' gluon mass of the order of 1 GeV and a gluon–gluon correlation length of about 0.3 fm. The pion mass scale is rather small, and more general 'boson' exchange is preferred. The weight factors of different mass scales take the impact parameter distribution of the particle opacity into account.

The role of inelastic channels in describing elastic scattering can be revealed by understanding the origin of and prescribing a definite shape to the overlap function $F(p, \theta)$ in the s-channel unitarity condition (18) or, equivalently, to its Fourier transform in the impact parameter picture. The scattering is mainly diffractive, i.e., it is due to the absorption of incoming waves in many open inelastic channels. Its quantitative field-theory treatment presents a serious unsolved problem.

The overlap function contains the sum of products of a matrix element of the inelastic process with a particular final state and the complex conjugate matrix element with the same final-particle content. However, their kinematical difference must be taken into account because the two final protons are scattered at an angle θ relative to the initial ones. Correspondingly, the overlap of the momentum distributions of the intermediate inelastic n-particle states is nontrivial kinematically and, what is especially important, the phases of these matrix elements become crucial. The phases are related to the position in space where particles are produced. It has been pointed out in many papers [125–128] that only the phase cancelation effect, which is closely related to particle correlations in inelastic processes, can lead to a realistic shape of the diffraction cone. The problem of properly accounting for them has not yet been solved.

At the same time, elastic scattering should be less peripheral because of a larger number of exchanged objects if regarded as an s-channel iteration of the overlap function. The great difficulty in transferring large momenta reveals itself already in the sharp shape of the forward diffraction peak. There have been numerous attempts to understand it in terms of the peripheral approach (see, e.g., [129–133]). Unfortunately, no framework for commonly accounting for both the s- and t-channel unitarity conditions has been developed.

In general, there have been many ideas proposed for describing elastic scattering processes, but no cogent theoretical arguments to justify the particular forms relying mainly on 'intuition' have been offered. The fact that they are very simple is usually the only advantage. Any strict interpretation is an idealization and as such should not be expected to be exactly true.

4.1.1 Geometry of the internal hadron structure. The key elements of the geometric approach are the use (a) of the impact parameter picture with Fourier–Bessel transformation (21), (22) from the transferred momenta amplitude to the spatial description, (b) of eikonal approximation (22), and (c) of unitarity condition (26). The S-matrix in the impact parameter picture is chosen in the exponential form

$$S(s, b) = \exp\left(-\Omega(s, b)\right), \tag{43}$$

and the convolution approximation for the real opacity Ω for elastic AB scattering is used:

$$\Omega(s, b) = K D_{\text{A}} \otimes D_{\text{B}}\,. \tag{44}$$

Here, $\otimes$ denotes the convolution of hadronic matter density distributions D for A and B, and K is an energy-dependent

factor. The assumptions about the validity of the eikonal approximation, the nearly imaginary character of the scattering amplitudes at low transferred momenta, the proportionality between the hadronic matter distribution and the electric charge distribution, the exponentiation of the S-matrix in b-space, and the validity of unitarity condition (26) are widely used.

The droplet model [134, 135] for elastic collisions was the first to fully exploit all the above elements. Particles were pictured as very much similar to nuclei. Correspondingly, the notion of the density distribution D inside a particle was introduced such that

$$\Omega(s,b) = \text{const} \int_{-\infty}^{+\infty} D\big((b^2 + x^2)^{1/2}\big)\,\mathrm{d}x\,. \tag{45}$$

In potential models, it corresponds to the WKB approximation. For the Gaussian shape of $h(s,b)$, it is possible to solve for D from (45), obtaining the function familiar in the theory of Bose–Einstein condensation of free particles [135]. In the droplet model, the disk properties are independent of the energy at sufficiently high energies. Many diffractive minima in the differential cross section have been predicted. The dipole form factors in the t-representation led to $\Omega(s,b)$ with a shape of the modified Bessel functions, which allowed fitting differential cross sections at ISR energies [136, 137]. The intuitive picture of high-energy hadron collisions as two extended objects breaking into fragments (and thus defining the overlap function!) has promoted the hypothesis of limiting fragmentation [138] inspired by the droplet model.

Models based on consideration of tower diagrams [50, 87] predict that the disk becomes larger and more absorptive as the energy increases. Both the black core and gray fringe expand with energy and become more absorptive.

The first estimates of the radii of protons, pions, and kaons from their form factors [139–141] showed that protons are larger than pions and kaons. This is not surprising, in view of the smaller cross sections of πp and Kp interactions than those of pp. The typical size is somewhat smaller than 1 fm. The proton hadronic matter distribution was fitted by a dipole form similar to the electric form factor but with the energy-dependent radius.

Other early attempts to consider the elastic scattering of hadrons also stemmed from the analogous simple geometric treatment of their internal structure [136, 137, 142–144]. Later, more complicated models were used. The main focus is, surely, on processes at small angles within the diffraction cone. They define the bulk contribution to the elastic scattering cross section due to the steep falloff of the distribution with increasing angles. Different models happen to fit the experimental data quite well in a wide energy range. But they fail outside the diffraction peak, as mentioned above. Large-angle scattering requires more central collisions with a lower impact parameter to probe the internal content of particles. Therefore, these regions of transferred momenta are discussed separately below.

Some ideas stemmed from regularities in inelastic processes. The multiplicity distributions of created particles are closely related to the purely geometric notion of the centrality of collisions. When the scaling of multiplicity distributions [146] was supported by experimental data, the proposal of the geometric scaling [145] for the elastic amplitude was promoted. The difficulties in accelerating the various parts of a nucleon without breaking it up had to be accounted for.

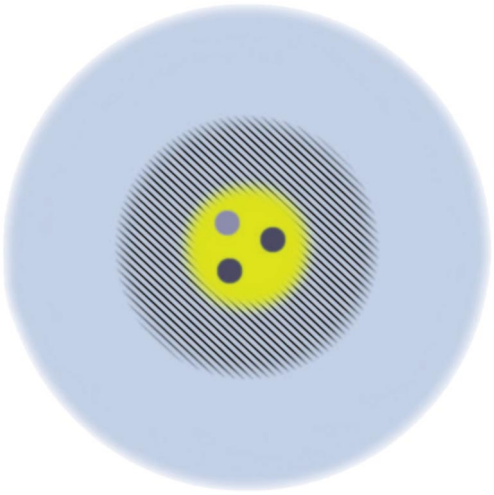

Figure 4. The nucleon structure according to the model in [63, 93, 94, 119]. The three regions of the internal structure are supposed to be directly responsible for the three regimes in the behavior of the differential cross section.

The basic idea of the geometric scaling is that at sufficiently high energies, the amplitude $A(s,t)$ depends on a single variable, the scaling parameter τ:

$$\tau = -\frac{t}{t_0}\ln^2\frac{s}{s_0}\,. \tag{46}$$

This idea has led to several predictions at asymptotically high energies, and is still actively being debated. Such scaling was proved [147, 148] for cross sections increasing as $\ln^2(s/s_0)$ and for an infinitesimally small ratio of the real to imaginary part of the amplitude $\rho \to 0$ as $s \to \infty$. The latest results on $\rho(s,t)$ discussed in Section 4.2.5 do not support this assumption.

The purely geometric standpoint is adopted in Refs [63, 93, 94, 119]. The three regions in the behavior of the differential cross section are clearly reflected in the three spatial scales of the internal hadronic structure considered in [93, 94, 119,104]. The authors of this three-scale model claim that the nucleon has an outer cloud of the quark–antiquark condensate, an inner shell of the baryonic charge density, and a still smaller internal core of massless color-singlet valence 'quarks' surrounded by low-x gluon clouds about 0.3 fm in size. This picture is shown in Fig. 4.

The diffraction cone is described as a result of cloud–cloud interaction, represented by a class of potentials containing the sum of modified Bessel functions. The least massive exchanged quanta are the most important ones. At larger momentum transfers, the baryonic charge at intermediate distances is probed by the ω-exchange. The internal region filled in by the valence quarks starts playing its role in the presence of even larger transferred momenta.

The diffraction profile function, which defines the range of different densities and, correspondingly, different forces, is taken to be

$$\Gamma(s,b) = 1 - \Omega(s,b) = g(s)\left[\frac{1}{1+\exp\left[(b-r)/a\right]} + \frac{1}{1+\exp\left[(-b+r)/a\right]} - 1\right]. \tag{47}$$

The parameters r and a are energy dependent,

$$r = r_0 + r_1\left(\ln\left(\frac{s}{s_0}\right) - \frac{\mathrm{i}\pi}{2}\right), \qquad a = a_0 + a_1\left(\ln\left(\frac{s}{s_0}\right) - \frac{\mathrm{i}\pi}{2}\right), \tag{48}$$

and $g(s)$ is a coupling strength; $s_0 = 1\ \mathrm{GeV}^2$.

These functions render the shape of the differential cross section, similar to the Fraunhofer diffraction (see Section 4.1.2), with the form factor proportional to $\pi dq/\sinh(\pi dq)$ ($q^2 = -t$, d is an adjustable parameter) proposed a long time ago [148–153]. This form factor also extends somewhat to transferred momenta outside the diffraction cone. Unfortunately, the contemporary phenomenological analysis of experimental data is not able to determine the impact parameter profiles unambiguously.

The scattering due to ω-exchange is parameterized by the product of the ω-propagator and two form factors F directly in the (s,t)-representation:

$$A_\omega(s,t) \propto s\exp\left(\mathrm{i}\chi(s,0)\right)\frac{F^2(t)}{m_\omega^2 - t}\,. \tag{49}$$

The amplitude due to quark–quark scattering has two 'structure factors' G of valence quarks (different from the above form factors): the propagator with the black disc radius r_B of qq asymptotic scattering and s-dependent factors with the hard Pomeron intercept equal to $1 + \alpha_\mathrm{h}$:

$$A_\mathrm{qq}(s,t) \propto \mathrm{i}s\exp\left(\mathrm{i}\chi(s,0)\right)\left[s\exp\left(-\frac{\mathrm{i}\pi}{2}\right)\right]^{\alpha_\mathrm{h}}\frac{G^2(t)}{r_\mathrm{b}^{-2} + |t|}\,. \tag{50}$$

In total, there are seventeen adjustable parameters in the model.

As mentioned in [49], the fits according to this model predict too low a value of the slope B at $|t| = 0.4\ \mathrm{GeV}^2$ and strongly disagree with experiment at 7 TeV outside the diffraction peak (see Fig. 2). Formulas (49) and (50) are aimed to improve the fit just in this region, but they do not help.

In general, an internal region of the nucleon where the gluons cluster around the original valence quarks resembles the valon model [154, 155]. Similar pictures arise in the QCD-inspired models discussed below.

Surely, some care should be taken for any such model to be accepted and the geometric picture to be considered seriously, especially in view of its success or failure to describe experimental data in the whole range of transferred momenta at various energies.

4.1.2 The modified Fraunhofer diffraction. For a long time (see, e.g., Ref. [156]), the formulas of classical diffraction of light on a (black or grey) disk with the traditional Bessel functions have been used for hadronic reactions. Recently, an analogous expression for the elastic amplitude was considered in Ref. [157]:

$$A\left(s, |t| = q^2\right) = C\,\frac{dq}{\sinh(\pi dq)}\left(\mathrm{i}\,\frac{J_1(Rq)}{Rq} + \frac{\rho}{2}\,J_0(Rq)\right). \tag{51}$$

The free parameters in arbitrarily chosen analytic expression (51) are C, R, d, and ρ. The first term resembles the expression for the black disk, Eqn (36). The suppression at large transferred momenta is assumed to be approximated by the form factor in front of the Bessel functions. In the impact parameter representation, this shape corresponds to the ordinary Fermi profile used, e.g., in Refs [93, 94, 119, 158] and shown in Eqn (47):

$$h(b) \propto \frac{1}{1 + \exp\left[(b - R)/d\right]}\,. \tag{52}$$

The second term in brackets in (51) takes the contribution due to the real part of the amplitude into account. It should smooth the behavior of the differential cross section near zeros of the first term. This seems to be the only difference from the first component of the previously discussed model [93, 94, 119].

And, again, comparison with experimental data shows that the results of fits are satisfactory in the diffraction cone, but not outside it. The form factor in front of common Bessel functions does not fit the large-$|t|$ trends of experimental distributions.

Throughout these developments, modifications of early guesses have been found necessary, but the general spirit of the geometric description remains immutable and viable.

4.1.3 Electromagnetic analogies. The strongly interacting content of hadrons is often considered to be similar to their electromagnetic substructure [136, 137]. Similarly to the droplet model, the assumption of the proportionality between the hadronic matter distribution and the electric charge distribution is used in many models. However, in most of them, the electromagnetic form factors are used in combination with Reggeon exchanges because, considered alone, they do not reproduce the energy dependence of the main characteristics. But the assumption about the full congruence of these distributions is not necessarily valid, since gluons do not carry an electric charge even though they play an important (if not decisive) role in high-energy strong interactions. That is why the charge and matter distributions in some models are parameterized separately or some corrections are added.

Using the experience from calculations of tower diagrams in electrodynamics and the impact-parameter representation, it was proposed [92, 159–161] that the possibility of choosing the opacity $\Omega(s,\mathbf{b})$ in a factored form be considered:

$$\Omega(s,\mathbf{b}) = R(s)\,F(\mathbf{b}^2) + (\text{nonleading terms})\,, \tag{53}$$

where $R(s)$ is chosen to be crossing symmetric under $s \leftrightarrow u$ and to reproduce the energy dependence of the Pomeron, considered as a fixed Regge cut,

$$R(s) = \frac{s^c}{(\ln s)^{c'}} + \frac{u^c}{(\ln u)^{c'}}\,, \tag{54}$$

while $F(\mathbf{b}^2)$ is taken as the Bessel transform of

$$F(t) = f\left|G(t)\right|^2\frac{a^2 + t}{a^2 - t}\,. \tag{55}$$

Here, $G(t)$ stands for the proton 'nuclear form factor', parameterized like the electromagnetic form factor with two poles:

$$G(t) = \frac{1}{(1 - t/m_1^2)(1 - t/m_2^2)}\,. \tag{56}$$

Other factors with the parameter a are introduced 'by hand'. They can be treated just as a correction due to the different shapes of distributions of charge and matter. There are six adjustable parameters in total used at high energies if the Regge background is neglected. The noticeable t-dependence of the slope $B(t)$ in the diffraction cone is predicted. However, its values at 7 TeV are lower than experimental ones (about 18 GeV^{-2} instead of 20.1 GeV^{-2}) at $10^{-2} < |t| < 0.3$ GeV^2, slightly exceed them in the tiny interval near 0.35 GeV^2, and do not reach the value 23.6 GeV^{-2} mentioned above.

This model is close to the TOTEM data [48, 49] for the dip position and the exponential at very large $|t|$, but predicts values of the differential cross section in the Orear range about twice as large, $|t| \geqslant 0.36$ GeV^2 (see Fig. 2). In addition to the dip, some 'oscillations' at the transferred momenta of several GeV^2 are predicted (up to the energy of 6000 TeV) but not yet observed. In general, such structures appear as a byproduct of the eikonal approach and unitarization procedure (see, e.g., Ref. [95]). Their energy dependence is strongly determined by the parameters used in formula (54) to account for the crossing symmetry property of the amplitude.

The same parameters are crucial for the behavior of the real part of the amplitude. It is interesting that the model predicts the dominance of the imaginary part of the amplitude even at large transferred momenta. The real part becomes important only at zeros of the imaginary part. The dip and oscillations are noticeable precisely there. Near the cone, the model predicts two zeros of the real part of the full (Coulomb + nuclear) amplitude at $|t| = 0.0064$ GeV^2 and the nuclear amplitude alone at $|t| \geqslant 0.18$ GeV^2, as well as one zero of the nuclear imaginary part at $|t| = 0.5$ GeV^2. In the differential cross section, the last zero is partly compensated by the real part.

We note the difference between the power-like expression for $F(t)$ and its exponential behavior in the traditional Regge models. The exponentiation of this form of $F(t)$ leads to additional oscillations.

A similar but more complicated combination of the form factors has been used in Refs [73, 74, 162–165]. The authors consider t-dependent Mellin transforms of parton distributions and claim that the first moment G defines the form factor of the standard Pomeron, while the second moment H corresponds to interaction attributed to three nonperturbative gluons. Thus, the behavior of the differential cross section is determined by the electromagnetic form factors at small t and by the matter distribution at large t. The Born term of the elastic scattering amplitude is written as

$$A^{\text{Born}}(s,t) = h_1 G^2(t) F_a(s,t)\left(1 + \frac{r_1}{\hat{s}^{0.5}}\right) + h_2 H^2(t) F_b(s,t)\left(1 + \frac{r_2}{\hat{s}^{0.5}}\right), \qquad (57)$$

where

$$F_a(s,t) = \hat{s}^{\epsilon_1} \exp\left(B(s)t\right), \qquad F_b(s,t) = \hat{s}^{\epsilon_1} \exp\frac{B(s)t}{4}, \qquad (58)$$

$$G(t) = \frac{L_1^4}{(L_1^2 - t)^2}\,\frac{4m_\text{p}^2 - 2.793t}{4m_\text{p}^2 - t}, \qquad H(t) = \frac{L_2^4}{(L_2^2 - t)^2}, \qquad (59)$$

$L_1^2 = 0.71$ GeV^2, $L_2^2 = 2$ GeV^2, $\hat{s} = s\exp(-\text{i}\pi/2)/s_0$, $s_0 = 1$ GeV^2, $B(s) = \alpha' \ln(s/s_0)$, and $\alpha' = 0.24$ GeV^{-2}. We note that the slope of the second term is chosen as one fourth that of the first term. The final form of the amplitude is obtained after eikonalization of the Born contribution using the opacity

$$\Omega(s,b) = \frac{1}{2\pi}\int \text{d}^2 q \, \exp(\text{i}\mathbf{qb})\, A^{\text{Born}} \quad (s, q^2 = -t). \qquad (60)$$

The total cross section at 7 TeV was predicted to be equal to 95 mb. Authors demonstrate good fits of pp and $\text{p}\bar{\text{p}}$ differential cross sections, as well as of $\rho_0(s)$, in a wide energy range, including the TOTEM data. Only five (three for high energies and two for low energies) adjustable parameters are claimed to be used if all the above values are regarded as fixed. In fact, there are 10 such additional 'hidden' parameters in total if the hard Pomeron is also considered. Surely, the contribution from secondary Reggeons at LHC energies is negligible, i.e., smaller than the experimental errors.

The real part of the hadron amplitude is completely determined by the complex expression for $\hat{s}$. Its t-dependence appears just as a byproduct of the eikonalization procedure. As a function of t, it tends to zero at $|t| \approx 0.16$ GeV^2 at the energy of 7 TeV. The interesting predictions of the t-behavior of $\rho(s,t)$ at nonforward transferred momenta for different energies are presented. They are discussed in more detail in Section 4.2.4.

4.1.4 Reggeon exchanges. The Regge-pole model is beyond dispute one of the most explored. It will have already been noticed that the notion of Regge trajectories has been used in the preceding subsections as well. The only reason to discuss these models separately there was their stronger inclination to the use of nonexponential electromagnetic form factors and geometric pictures in the s-channel approach. At the same time, Reggeon models appeal mostly to the t-channel approach.

The amplidutes with Reggeon exchanges in the t-channel are natural candidates for explaining the exponential decrease in differential cross section (6) with the squared transferred momentum $|t|$ inside the diffraction cone. Just this shape is typical for them because it follows from the linearity of Regge trajectories. Moreover, they predict a logarithmic increase in the hadronic radii as the energy increases, i.e., a logarithmic increase in the cone slope B or the corresponding shrinkage of the width of the diffraction cone. This prediction is also supported by experiment. In the common Regge-pole models, the disk becomes larger and slightly more transparent as energy increases.

The standard Regge-type models [73, 74, 97, 166, 167] use the combination of contributions due to the exchange by the (multicomponent) Pomeron, Odderon, and secondary Reggeon trajectories corresponding to f and ω mesons with or without the form factors chosen in a simple exponential form or as power-like expressions resembling the electromagnetic structure of colliding partners discussed in the preceding subsection. The price to be paid is the increased number of adjustable parameters at each step of sophistication. To be more or less realistic, one has to use the knowledge about some of them from other (independent?) experimental results. But even under this condition, the ambiguity of their choice and sensitivity to fitted parameters leave some freedom in the conclusions.

The amplitudes of pp and $\text{p}\bar{\text{p}}$ scattering are approximated by the sum of terms corresponding to the leading (Pomeron and Odderon) and nonleading (f and ω meson) Regge

trajectories:

$$A(s,t)_{\mathrm{p\bar{p}}}^{\mathrm{pp}} = A_{\mathrm{P}}(s,t) + A_{\mathrm{f}}(s,t) \mp \left(A_{\omega} + A_{\mathrm{O}}(s,t)\right), \qquad (61)$$

where the labels P, f, O, and ω stand for the relevant contributions. The sign in the pp and p$\bar{\mathrm{p}}$ amplitudes differs for C-even and C-odd terms.

The contributions of the nonleading Regge poles are written as

$$A_{\mathrm{R}}(s,t) = a_{\mathrm{R}} \exp\left(-\frac{\mathrm{i}\pi\alpha_{\mathrm{R}}(t)}{2}\right) \exp\left(b_{\mathrm{R}} t\right) \left(\frac{s}{s_0}\right)^{\alpha_{\mathrm{R}}(t)}, \qquad (62)$$

with $\alpha_{\mathrm{R}}(t) = a_{\mathrm{R}} + b_{\mathrm{R}} t$.

While the secondary trajectories are usually chosen in a standard linear way, the Pomeron and Odderon contributions can be regarded, for example, as dipoles with nonlinear trajectories [166, 168–171]:

$$A_{\mathrm{P}}(s,t) = \mathrm{i}\,\frac{a_{\mathrm{P}} s}{b_{\mathrm{P}} s_0} \left\{ r_1^2(s) \exp\left[r_1^2(s)(\alpha_{\mathrm{P}} - 1)\right] - \epsilon_{\mathrm{P}} r_2^2(s) \exp\left[r_2^2(s)(\alpha_{\mathrm{P}} - 1)\right] \right\}, \qquad (63)$$

where $r_1^2(s) = b_{\mathrm{P}} + L - \mathrm{i}\pi/2$ and $r_2^2(s) = L - \mathrm{i}\pi/2$ with $L = \ln(s/s_0)$. The unknown Odderon contribution is assumed to be of the same form as that of the Pomeron. The parameters of the trajectories and of the absorption ϵ_P have to be adjusted. Their nonlinearity may be connected with the two-pion threshold following from the t-channel unitarity [168, 170, 172]. However, there could be double counting of the graphs with Pomerons attached on both sides to the pion loop. This is well known from old peripheral models of inelastic processes, where the self-consistent Bethe–Salpeter equation had to be used for the proper account of the pion–nucleon vertices. Different forms of nonlinear trajectories are in use. For instance, the Pomeron trajectory is chosen in [173] with four free parameters as

$$\alpha(t) = \alpha_0 - \gamma \ln\left(1 + \beta\sqrt{t_0 - t}\right). \qquad (64)$$

A more complicated nonlinearity was used in [172]. However, the use of the pion mass as a scale there is questionable in view of the above discussion.

The origin of the Pomeron and the parameterization of its trajectory are still being debated. There is no strict rule for choosing its shape. The dipole and even tripole forms of unitarized Pomerons have been attempted. They mimic cut contributions [174–177].

Moreover, there are arguments in favor of two Pomerons with different intercepts. Even the fits with three Pomerons are sometimes used [79, 97]. The soft Pomeron contributes a term with the energy dependence $s^{a_{\mathrm{s}}}$ ($a_{\mathrm{s}} \approx 0.08$) to hadron–hadron total cross sections, and the hard Pomeron makes a small contribution (at present energies) with a stronger energy dependence $s^{a_{\mathrm{h}}}$ ($a_{\mathrm{h}} \approx 0.4$). These values of the intercepts stem from the discussions of HERA data (see, e.g., [178]). Although the hard-Pomeron exchange was unnecessary for describing hadron–hadron total cross sections up to the energies $\sqrt{s}$ below 1 TeV, it may reveal itself at LHC energies, as argued in [179]. The model in [179] uses only two terms in the expansion for opacity:

$$\Omega(s,b) = \Omega_{\mathrm{s}}(s,b) - \frac{\lambda}{2}\,\Omega_{\mathrm{s}}^2(s,b), \qquad (65)$$

where Ω_{s} stands for the contribution from single exchanges of Reggeons (two Pomerons, f, and ω) with the adjustable parameter λ, as well as for the triple-gluon exchange of the form Cst^{-4} needed at larger values of $|t|$ and matched at some $t = t_0$ to exponential shapes of the diffraction peak and to the dip region. Certainly, adding such a term allows fitting the total cross section value at 7 TeV, but there is a suspicion that the sharp increase in the hard-Pomeron contribution will overpredict the cross sections at higher energies. The unitarization will become mandatory once again. The quality of the fit of the differential cross section beyond the diffraction peak is no better than of the fits shown in Fig. 2.

Several variant forms of Born amplitudes and different kinds of eikonalization have been attempted. There is no consensus on their choice.

A form of the eikonal similar to (65) is chosen in [180] with the exponential suppression

$$\Omega_{\mathrm{s}}(s,b) = A_0 \exp\left[-m(s)(r_0^2 + b^2)^{1/2}\right] \qquad (66)$$

for central interactions. The peripheral part of the Pomeron interaction with the meson cloud is parameterized [180] by a small term increasing with the energy and resulting in a $\sqrt{|t|}$ exponential fall-off of the differential cross section. The geometric picture corresponds to a black disk with a gray fringe, similarly to the above-described model [92].

In general, it is not easy to estimate the total number of adjustable parameters in different models. There are parameters related to either t- (b-) or s-dependence. In some papers, it is often assumed that part of them are known from fits of other characteristics of hadron or electromagnetic interactions at various energies and can therefore be considered known beforehand. For example, it is claimed that the model in [166] contains about 15 parameters. In this case, it is quite difficult to find the proper minima for the matrix of χ^2 values. It is well known how unstable the final results can be: one has to choose a step-by-step procedure for doing this and use some special computer codes.

There are 25 adjustable parameters shown in Table 1 in papers [79, 97]. However they include some values assumed to be *a priori* fixed in [166]. At the same time, additional form factors were inserted in the formulas, albeit with preliminarily 'fixed' parameters. They were used to fit 982 pp and p$\bar{\mathrm{p}}$ data points in a wide energy range. Besides the elastic differential cross sections, the total cross sections and the ratios ρ_0 were considered. The fit in the interference region of Coulomb and hadronic amplitudes with the same parameters helped in choosing among the different Coulomb phases proposed previously.

A similar situation is seen in the fits in Ref. [73, 74], where it is claimed that the number of parameters is much less (only 5!). However, there are many other, hidden parameters (in particular, those concerning the energy behavior and form factors). They are held fixed from the very beginning, as was discussed in Section 4.1.3.

As mentioned above, the simple exponential form of the differential cross section in the diffraction cone is quite well described. This becomes possible mainly due to the t-shape of the Pomeron trajectory in (63) and other Reggeons contributions in (62). The fits in this region at the different energies, shown, e.g., in [73, 74, 97, 166], are quite impressive. The evolution of the diffraction cone slope with energy is reproduced [as described by L in (63)]. Unfortunately, the variety of forms of Pomeron trajectories with different

intercepts, slopes, and shapes of residues unitarized in different ways and/or substituted by Regge cuts is so large that it is impossible to show all of them in this review due to the limited space.

The cuts with nonlinear trajectories mimic hard scattering [98]. A common problem appears in predicting them at larger angles. The fit according to the model in [79, 97] seems to be most successful in predicting the position of the dip and the shape at large $|t|$, but exceeds the absolute value approximately twofold. The model in [166] strongly underestimates it, with the wrong position of the dip and much slower decrease at $|t| > 1.5$ GeV^2. This is well demonstrated in Fig. 2 and is also discussed below.

We mention that all these papers follow the general approach proposed much earlier [170, 181–183]. They just deal with more detailed fits of newly available experimental data.

4.1.5 QCD-inspired models. Each incident particle consists of a superposition of Fock states with n partons [184], which are scattered instantaneously and simultaneously by the other particle. Some QCD-inspired models using this statement have been developed. The role of partons is played by quarks and gluons.

The two competing mechanisms of hadron interactions, the increase in the density (α in Table 1) and in the radius R, determine their specific features. In QCD, they can be respectively ascribed to the leading-order solution of the BFKL equation [185, 186] and to the long-range (Weizsäcker–Williams) nature of the field of massless gluons. The density increase due to the BFKL evolution leads to a power-law increase in the total cross section, which is nonunitary and violates Froissart bound (31). Therefore, at the critical density of the order $1/\alpha_s$, the density saturation must be taken into account [187]. The QCD evolution in all orders in the gluon density but in the leading logarithmic approximations is treated by the JIMWLK equations [188]. With account of multiple scattering effects, they can be simplified in the large-N_c limit to a single nonlinear BK equation for the gluon density [189, 190] when the induced field density is small.

The density growth effects are preasymptotic. According to [100], they are described by a hard Pomeron, while the growth of the size of the black saturated regions (the radius) is attributed to a soft Pomeron. The hard Pomeron manifests itself in small systems or in small subregions inside hadrons. The soft Pomeron appears in hadronic systems of a typical size and is related to an increased size in the impact parameter space. Only the increase due to the perturbative expansion in the transverse plane remains effective.

There is no consensus about this scenario proposed in Ref. [100]. The soft Pomeron is often used [80, 81, 191, 192] in attempts to explain the preasymptotic power-law growth of cross sections by an additional nonperturbative mechanism superimposed on the BFKL scenario of a hard Pomeron. It is ascribed mainly to the density growth of gluon clouds around quarks and not to the spatial scale of the interaction. Even though the size of gluon clouds increases, it is still limited by a short separation from their source. The proton looks like three valence quarks surrounded by gluon clouds or spots with mean sizes about 0.3 fm smaller than the proton radius, of the order of 1 fm. Radiation from any additional gluon in the cloud adds the factor $\ln(s/s_0)$ to the interaction cross section, and hence their sum gives a power-like term of the form

$$\sigma_t = \sigma_0 + \sigma_\Delta \left(\frac{s}{s_0}\right)^\Delta , \qquad \Delta = \frac{4\alpha_s}{3\pi} \approx 0.17 , \tag{67}$$

with a large constant term σ_0 and small σ_Δ. Using the standard dipole form factors of protons and quasi-eikonal unitarization in the impact parameter space, the authors of this two-scale model [80, 81, 192] fit many distributions with 10 parameters for the t-dependence (subject to two additional constraints) and some parameters for the s-dependence. Such fits are, of course, aimed at high energies of colliding protons where the effects of secondary Regge trajectories die out. They are mainly successful in the diffraction cone and, consequently, in describing the energy dependence of the total and elastic cross sections.

Such a form of the total cross section with an energy-independent term σ_0 was proposed a long time ago [193–195] and actively developed later [196–198] in the framework of the parton model and semihard QCD, with the gluon–gluon interaction playing the main role.

The main role of gluons is also incorporated in [99, 110]. The profile is chosen in a form containing the gg, qq, and qg terms:

$$\Omega = \sigma_{gg} W(b;\mu_{gg}) + \Sigma_{gg}\left(C + C_R \frac{m_0}{s^{1/2}}\right) W(b;\mu_{qq}) + \Sigma_{gg} C_{qg} \ln\frac{s}{s_0}\, W\bigl(b;(\mu_{qq}\mu_{gg})^{1/2}\bigr) , \tag{68}$$

where the impact parameter distribution functions are

$$W(b;\mu) = \frac{\mu^2(\mu b)^3 K_3(\mu b)}{96\pi} , \tag{69}$$

and the gluon–gluon interaction cross section is

$$\sigma_{gg} = C_{gg} \int \Sigma_{gg} \Theta(\tau s - m_0^2)\, F_{gg}(\tau)\, d\tau , \tag{70}$$

with $\Sigma_{gg} = 9\pi\alpha_s^2/m_0^2$, $F_{gg} = \int f_g(x_1) f_g(x_2) \delta(\tau - x_1 x_2)\, dx_1\, dx_2$, and $f_g(x) = N_g(1-x)^5/x^{1+\epsilon}$.

The Froissart bound for the total cross section is reproduced with

$$\sigma_t = 2\pi \left(\frac{\epsilon}{\mu_{gg}}\right)^2 \ln^2\frac{s}{s_0} . \tag{71}$$

The parameter μ_{gg} describes the area occupied by gluons in the colliding protons (the size effect), and ϵ is defined via their gluonic structure functions and therefore controls their soft gluon content (the density effect).

Again, being successful in the diffraction peak with its shape and normalization, the model in [99, 110] fails to predict the correct behavior of the differential spectrum outside it [48, 49]. Its prediction is more than three times larger than the experimental value at the dip and the subsequent maximum, while falling too steeply at ever higher $|t|$ above 1.5 GeV^2 (see Fig. 2).

Attempts to consider the semihard scattering of quarks and gluons can be found in Refs [197–201].

The traditional partonic description of the process is considered in a series of papers [172, 202–204]. The partonic approach with a hard BFKL Pomeron can be merged into the domain governed by the soft Pomeron. The transition from hard to soft is induced by absorptive multi-Pomeron effects in a limited energy range. The evolution produces parton

cascades, not strongly ordered in transverse momenta, with hot spots of a relatively small size in b-space. The saturation is driven by the enhanced multi-Pomeron graphs, also regulating the high-mass dissociation. The calculations are done with a 3-channel quasi-eikonal unitarization using the opacity formalism. They reproduce the shapes of the differential cross sections from ISR to LHC energies within the diffraction cone.

Another picture was considered in the framework of the functional integral approach in Refs [205–208] using the model of the stochastic vacuum and making the assumption that the proton has the quark–diquark structure of a color dipole, i.e., two quarks out of three are close together in transverse directions. A matrix cumulant expansion is used for vacuum expectation values of Wegner–Wilson loops [205] related to hadronic amplitudes. The QCD vacuum parameters (the gluon condensate or the string tension, the vacuum correlation length, and the parameter due to the non-Abelian tensor structure), as well as the hadron size, have been used. The imaginary part of the amplitude in the b-representation was calculated. Its contribution to experimentally measured quantities was shown to describe the ISR and Tevatron data in the diffraction peak reasonably well.

A more phenomenological approach to the quark–diquark model was attempted in Refs [209, 210]. As above, the correlated quark and diquark constituents are considered. According to the detailed analysis performed in [211], from ISR to LHC energies in the range $0.36 < |t| < 2.5$ GeV^2, the model is able to describe the data quite well, even outside the diffraction peak, except the narrow strip around the dip. But it shows a much stronger dip (by several orders of magnitude) there than the experimentally observed one. Moreover, similarly to the abovementioned calculations, the model ignores the contributions to the real part of the elastic scattering amplitude. As we saw previously, such contributions can smooth this dip. If so, their shape should drastically differ from that of the imaginary part, at least in this strip, as happened, for example, in the models with electromagnetic form factors [92, 165].

4.2 Intermediate angles: the dip and the Orear regime

As long ago as the 1960s, experiments on elastic pp and πp scattering at comparatively low energies between 6.8 and 19.2 GeV in laboratory system [2, 9–11] showed that the steep exponential fall-off of the differential cross section as a function of the squared transferred momentum $|t|$ is replaced by a slower dependence at larger $|t|$. They showed that just after the diffraction cone a shoulder was observed and, even more surprising, a behavior exponentially decreasing with the angle or with $\sqrt{|t|}$, which was called the Orear regime after its investigator [5, 6, 9]. A special session was devoted to these findings at the 1968 Rochester conference in Vienna. The shoulder evolved later into a minimum or dip at higher ISR energies. It has also been observed at the LHC, as seen in Figs 2 and 3.

It is interesting that at the FNAL–ISR energies $\sqrt{s} = 6$–60 GeV, the exponential fall-off with an increase in $\sqrt{|t|} \approx p_t$ was observed up to quite large values $|t| \approx 10$ GeV^2 [20, 28, 45], with the exponent in the range from 6.2 to 7 GeV^{-1} (see Table 7 in Ref. [45]). It is even larger at the LHC (about 8–9 GeV^{-1}). The region becomes narrower and shifts to lower values of $|t|$ from 0.5 to 1.5 GeV^2. The power-like regime already shows up at about $|t| \approx 2-2.5$ GeV^2 (see Fig. 3).

4.2.1 Gaussian fits. From the very beginning, it was noticed [5, 6] that it is possible to fit the differential cross sections at intermediate values of the momentum transfer by an exponential dependence on $\sqrt{|t|}$ (or θ) except the relatively small shoulder region. To take that into account as well, it was primarily proposed [3] to use fits with Gaussian functions with alternating signs of the coefficients directly in the expression for the amplitude. In this way, both the diffraction peak and larger-$|t|$ behavior could be described. No reference to any phenomenological model is given. From the geometrical standpoint, one can imagine an internal structure with envelopes of alternating density.

Such an empirical approach has been used [212–214] for fits of experimental data at ISR energies. The following parameterization of the amplitude is proposed in Ref. [214]:

$$A(s,t) = s\left[\left(\rho\sigma_t - \sum_{i=2}^{m} 4\pi a_i\right)\exp(b_1 t) + \sum_{i=2}^{m} 4\pi a_i \exp(b_i t) + i\left(\sigma_t - \sum_{j=2}^{n} 4\pi c_j\right)\exp(d_1 t) + i\sum_{j=2}^{n} 4\pi c_j \exp(d_j t)\right], \quad (72)$$

where $m < n$. The fits at different energies give information about the ratio of the real to imaginary part of the amplitude $\rho(t)$, besides the values of adjustable parameters a_i, b_i, c_j, and d_j. Two different methods were used. In total, there are 14 to 16 free parameters. The results of nonlinear fits are rather unstable, and the conclusions are somewhat controversial. In particular, the numbers of zeros of $\mathrm{Im}\, A(s,t)$ and $\mathrm{Re}\, A(s,t)$ differ in these methods. The dominance of the real part of the amplitude at intermediate values of the momentum transfer in one of the methods is not confirmed when the other method is used.

A similar fit was recently attempted and applied to the TOTEM data in Refs [111, 215]. The earlier proposal in Ref. [216] with phenomenologically chosen two t-exponentials and the relative interference phase responsible for the dip was applied to the TOTEM data. Using five parameters, it is possible to describe these data in the whole range of transferred momenta. We note that similarly to the model in [165], the slope of the second exponential term is chosen several times smaller than that of the main term. Moreover, when the electromagnetic form factors were tried in place of simple exponentials, the fit became worse.

Two exponentials without the interference term inside the diffraction peak and a Tsallis-type distribution outside it were used in [217]. It was possible, with the help of nine free parameters, to fit the data at energies from 19.4 GeV to 7 TeV.

In some way, this fit business with no reference to any theoretical model looks more like art than science, especially if no conclusions about the hadron structure are obtained. Such an approach will hardly be conclusive in the future.

4.2.2 Phenomenological models. Theoretical indications of the possibility of a new regime with an increase in transferred momentum were obtained even earlier [56, 122, 218]. It was treated as a consequence of the simple iteration of processes approximated by a Gaussian within the diffraction cone. The term I_2 in unitarity condition (18) with Gaussians inserted into the integrand gives rise to a Gaussian with a width that is twice as big, i.e., to a shape twice as wide as the diffraction

cone. Further iterations lead to further widening. Therefore, multiple exchanges were considered. However, the results did not fit new experimental findings. This failure was explained as resulting from the improper treatment of the unitarity requirements and incorrect choice of the overlap function.

The droplet-model relations between form factors and the elastic amplitude for hadronic scattering at infinite energy (see Eqns (1) and (2) in Ref. [219]) predict a series of kinks (or zeros) in the differential cross section, which could be related to dips. Dip position movement to lower $|t|$ with a growth of the total cross section was predicted in Ref. [220]. There is also an indication of several dips (or shoulders) at larger $|t|$ in the models in [92, 165, 197, 198] using the electromagnetic form factors with subsequent eikonalization (cf. Figs 2 and 11).

In accordance with the experimental data shown in Fig. 2, only one dip is predicted by other models. For example, it was described in Ref. [221] on the basis of a modified optical model [220]. In the framework of the geometric scaling approach [222], the numerical integration of the relation

$$\frac{\mathrm{d}\sigma}{\mathrm{d}t}(s,t)\left(\frac{\mathrm{d}\sigma}{\mathrm{d}t}(s,0)\right)^{-1}=\frac{1}{1+\rho_0^2}\left[\phi^2(\tau)+\rho_0^2\left(\frac{\mathrm{d}\bigl(\tau\phi(\tau)\bigr)}{\mathrm{d}\tau}\right)^2\right], \tag{73}$$

where

$$\operatorname{Im}A(s,t)=s\sigma_{\mathrm{t}}\phi(\tau)\,,\qquad \phi(0)=1\,, \tag{74}$$

was performed with τ defined by Eqn (46).

It was predicted that the dip should even disappear at energies higher than $\sqrt{s}\approx 300$ GeV, but can reappear at ever higher energies. As we know now, it is clearly seen at 7 TeV. The imaginary part has been chosen in such a way that it has a zero at the dip. The absence of additional dips is explained as a deviation of the eikonal from a simple Gaussian with some flattening at small impact parameters (see Section 4.2.3). That shows strong sensitivity to the choice of tiny details of the phenomenological eikonal and also agrees with the properties of the overlap function to be discussed in more detail below. These results were confirmed and extended to $\mathrm{p\bar{p}}$ collisions in Ref. [223].

Processes described by diagrams with multiple exchanges by Pomerons are claimed to be responsible for the Orear regime at intermediate angles according to Refs [224, 225]. The differential cross section is predicted to have the form

$$\frac{1}{C}\frac{\mathrm{d}\sigma}{\mathrm{d}t}=\exp\left[-2\sqrt{2\pi\alpha'(0)|t|\xi\cot\frac{\phi}{2}}\,\varphi_1(\xi)\right]\times\left[1+\lambda\cos\left(2\sqrt{2\pi\alpha'(0)|t|\xi\tan\frac{\phi}{2}}+\varphi_0\right)\right], \tag{75}$$

where $\xi=\ln(s/4m^2)$, and C, ϕ, φ_0, φ_1, λ, and $\alpha'(0)$ are adjustable parameters. There are oscillations directly imposed on the exponential fall-off with the same exponential. They should be well pronounced. So far, no such oscillations have been observed.

A less strong statement about some saturation of the diffraction cone due to multiple Pomeron exchanges is made in Refs [226, 227].

4.2.3 Unitarity condition. A theoretical explanation based on the consequences of the unitarity condition in the s-channel has been proposed in Refs [57, 58]. The careful fit to experimental data showed good quantitative agreement with experiment [59]. Nowadays, the same approach helps explain the TOTEM findings [60] (see Fig. 5 below).

We consider the left-hand side and the integral term I_2 in unitarity condition (18) at the angles θ outside the diffraction peak. Because of the sharp fall-off of the amplitude with the angle, the leading contribution to the integral arises from a narrow region around the line $\theta_1+\theta_2\approx\theta$. Therefore, one of the amplitudes should be inserted at small angles within the cone as a Gaussian, while the other is kept at angles outside it. Integrating over one of the angles yields the linear integral equation

$$\operatorname{Im}A(p,\theta)=\frac{p\sigma_{\mathrm{t}}}{4\pi\sqrt{2\pi B}}\int_{-\infty}^{+\infty}\mathrm{d}\theta_1\,\exp\left[-\frac{Bp^2(\theta-\theta_1)^2}{2}\right]\times f_\rho\operatorname{Im}A(p,\theta_1)+F(p,\theta)\,, \tag{76}$$

where $f_\rho=1+\rho_0\,\rho(\theta_1)$. It can be solved analytically (see [57, 58] for more details) under two assumptions: that the role of the overlap function $F(p,\theta)$ is negligible outside the diffraction cone and the function f_ρ can be approximated by a constant, i.e., $\rho(\theta_1)=\rho_1=\mathrm{const}$. Both assumptions are discussed in the next subsections.

It is easy to verify that the eigensolution of this equation is

$$\operatorname{Im}A(p,\theta)=C_0\exp\left(-\sqrt{2B\ln\frac{Z}{f_\rho}}\,p\theta\right)+\sum_{n=1}^{\infty}C_n\exp\left[-(\operatorname{Re}b_n)\,p\theta\right]\cos\left(|\operatorname{Im}b_n|\,p\theta-\phi_n\right), \tag{77}$$

with

$$b_n\approx\sqrt{2\pi B|n|}\,(1+\mathrm{i}\,\mathrm{sign}\,n)\,,\qquad n=\pm1,\pm2,\ldots \tag{78}$$

This expression contains the term exponentially decreasing with θ (or $\sqrt{|t|}$) (Orear regime) with oscillations strongly damped by their own exponential factors. These oscillating terms are responsible for the dip. Just this formula was used in Refs [59, 60] for fits of experimental data in a wide energy range. The ratio ρ was approximated by its average values in and outside the diffraction cone, with $f_\rho=1+\rho_0\,\rho_1$, where ρ_1 is treated as the average value of ρ in the Orear region. The fits at comparatively low energies [59] are consistent with $f_\rho\approx 1$, i.e., with small values of ρ_l close to zero. The great surprise of the fit of TOTEM data in [60], shown in Fig. 5, was the necessity of using the negative value $\rho_1\approx -2.1$ large in modulus.

Being model-independent, this solution suffers from some limitations that are inherent for the unitarity relation in general and for unitarity equation (76) in particular. First, it predicts the dependence on transferred momenta $p\theta\approx\sqrt{|t|}$ but not the dependence on the collision energy. Second, it is applicable in a restricted (and not rigorously defined) range of angles in the Orear region.

The elastic scattering differential cross section outside the diffraction cone (in the Orear regime region) is

$$\frac{1}{p_1}\frac{\mathrm{d}\sigma}{\mathrm{d}t}=\left[\exp\left(-\sqrt{2B|t|\ln\frac{4\pi B}{\sigma_{\mathrm{t}}f_\rho}}\right)+p_2\exp\left(-\sqrt{2\pi B|t|}\,\right)\cos\left(\sqrt{2\pi B|t|}-\phi\right)\right]^2. \tag{79}$$

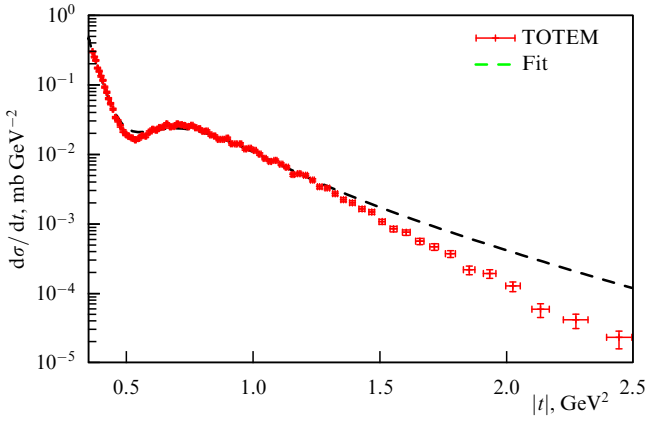

Figure 5. The fit of the differential cross section of elastic proton–proton scattering at $\sqrt{s} = 7$ TeV in the region beyond the diffraction peak according to the predictions of the unitarity condition [60]. Dots show experimental data, the line is the theoretical approximation.

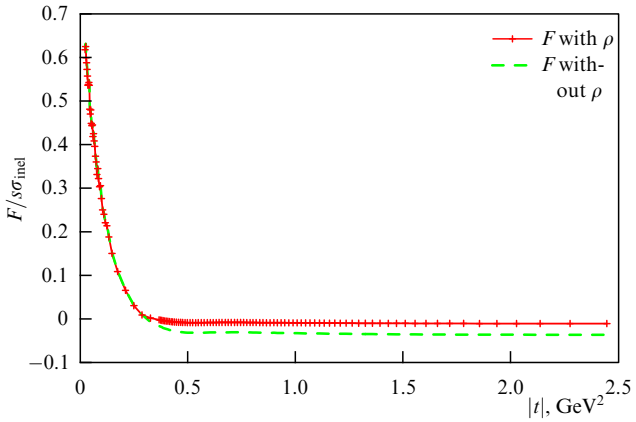

Figure 6. The overlap function at $\sqrt{s} = 7$ TeV obtained from the unitarity condition with substitution of experimental data on the differential cross section [60]. It is large in the diffraction cone and negligibly small outside it. The line nearest to the abscissa axis takes the real part of the amplitude into account, the farthest line is computed with $\rho = 0$.

It has been used in the fit in Fig. 5. Only the very first oscillating term in (77) is taken into account in this expression, because other terms are more strongly damped with $|t|$. It is important that the experimentally measured values of the diffraction cone slope B and the total cross section σ_t of the same experiment mostly determine the shape of the elastic differential cross section in the Orear region of transition from the diffraction peak to large-angle parton scattering. The value $Z = 4\pi B/\sigma_t$ is so close to 1 at 7 TeV that the fit is extremely sensitive to f_ρ because $\ln(Z/f_\rho)$ in the first term determines the slope in this region. Therefore, it becomes possible for the first time to estimate the ratio ρ_l outside the diffraction cone directly from fits of experimental data.

Moreover, it was mentioned in footnote 2 in Ref. [58] that Eqn (76) is in fact an equation for $\theta^{1/2}\mathrm{Im}\,A(p,\theta)$. The factor $\theta^{1/2}$ was omitted in this review and all previous papers because it was assumed that "retaining it would exceed the accuracy of the derivation" of the equation. However, it will be worthwhile to take it into account in the future, multiplying the right-hand side of (79) by $|t|^{-1/4}$. This would slightly improve the fit in Fig. 5.

We note that this shape of differential cross section (79) differs from formula (75), first of all, because of the suppression of oscillations by the exponential factors in front of them, which decrease much more strongly than the leading exponential. In (75), the exponential is common for the main and oscillating terms, while in (79), the oscillations are strongly damped. They may give rise to the dip adjusted to the diffraction cone if their amplitude is sufficiently large. The small secondary damped oscillations at larger values of $|t|$ have been seen at comparatively low energies (see Ref. [59]) but have not yet been noticed at the LHC. We stress that fit (79) contains only three adjustable parameters: the overall normalization p_1, the amplitude of oscillations p_2, which determines the depth of the dip, and f_ρ, which helps find the ratio ρ_l outside the diffraction peak from the slope of the differential cross section there.

4.2.4 Overlap function and the eikonal. Both the overlap function and the eikonal are subject to the unitarization procedure, albeit in somewhat different approaches. Therefore, it is instructive to compare their different forms.

We discuss what shapes of the overlap function can be considered as suitable for further use. One of the assumptions used in solving the unitarity equation was the smallness of $F(p,\theta)$ in the Orear region. The results in [60, 228] give strong support to the validity of this assumption. The overlap function was calculated there directly from experimental data, by subtracting the elastic contribution I_2 from the left-hand side of the unitarity equation without appeal to any model. It is described by the formula

$$F(p,\theta) = 16p^2\left(\frac{\pi\,\mathrm{d}\sigma/\mathrm{d}t}{1+\rho^2}\right)^{1/2} - \frac{8p^4 f_\rho}{\pi}\int_{-1}^{1}\mathrm{d}z_2\int_{z_1^-}^{z_1^+}\mathrm{d}z_1\left(\frac{\mathrm{d}\sigma}{\mathrm{d}t_1}\frac{\mathrm{d}\sigma}{\mathrm{d}t_2}\right)^{1/2}K^{-1/2}(z,z_1,z_2)\,, \qquad (80)$$

where $z_i = \cos\theta_i$, $K(z,z_1,z_2) = 1 - z^2 - z_1^2 - z_2^2 + 2zz_1z_2$, and $z_1^\pm = zz_2 \pm [(1-z^2)(1-z_2^2)]^{1/2}$. The result at 7 TeV is shown in Fig. 6.

Certainly, the shadow of inelastic processes represented by the overlap function dominates within the diffraction peak. But it is extremely small outside. It is even smaller at the LHC energies [50] than at lower ones [228], where a similar behavior of the overlap function at large $|t|$ was observed previously. Hence, this assumption is well founded.

Moreover, it is quite understandable that $F(s,t)$ is very small at large $|t|$ in Fig. 6. This shows that its fit by the solution of the unitarity relation has been done by the proper eigenfunction (77) with the correct eigenvalues of the integral equation.

It is tempting to solve nonlinear inhomogeneous unitarity equation (18) by iterations. That has been attempted several times [56, 58, 122, 218]. The main problem is the choice of the overlap function. The simplest ansatz is the Gaussian form at all transferred momenta. The argument in favor of it is just that it plays the decisive role in the diffraction cone, where the elastic amplitude has a Gaussian shape. But the results fail to describe the Orear regime. This may be ascribed to the role of phases of inelastic processes that determine the genuine shape of the overlap function, and/or to the improper approximation of ρ by a constant outside the diffraction cone. Again, similarly to the situation in the b-representation, the tiny details of the shape prevent the proper outcome. No

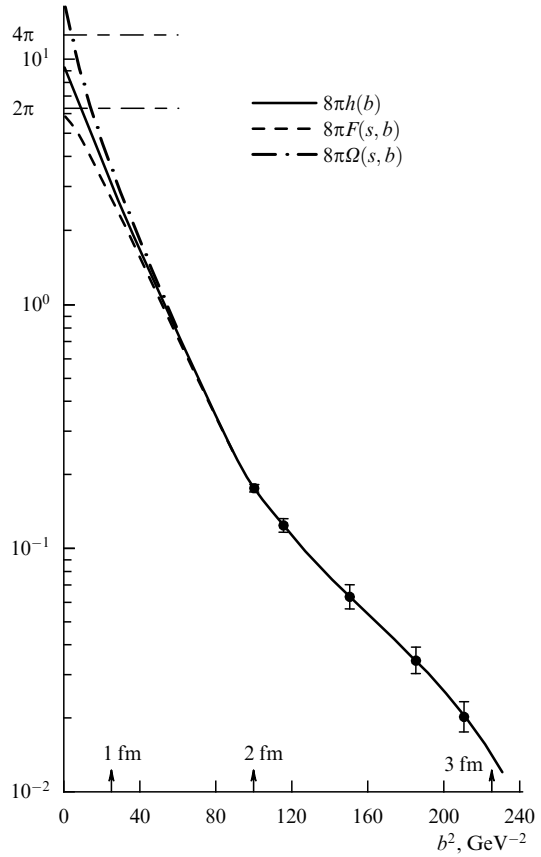

Figure 7. The shapes of the amplitude, overlap function, and eikonal extracted from experimental data at $\sqrt{s} = 52.8$ GeV as functions of the impact parameter squared (borrowed from [229]). In the notation of this review, the amplitude is $h(b) = \tilde{M}(b)/8\pi$, the overlap function is $F(s,b) = \tilde{O}(b)/8\pi$, and the eikonal is $\Omega(s,b) = \tilde{E}(b)/8\pi$. The corresponding spatial scales are shown on the abscissa axis.

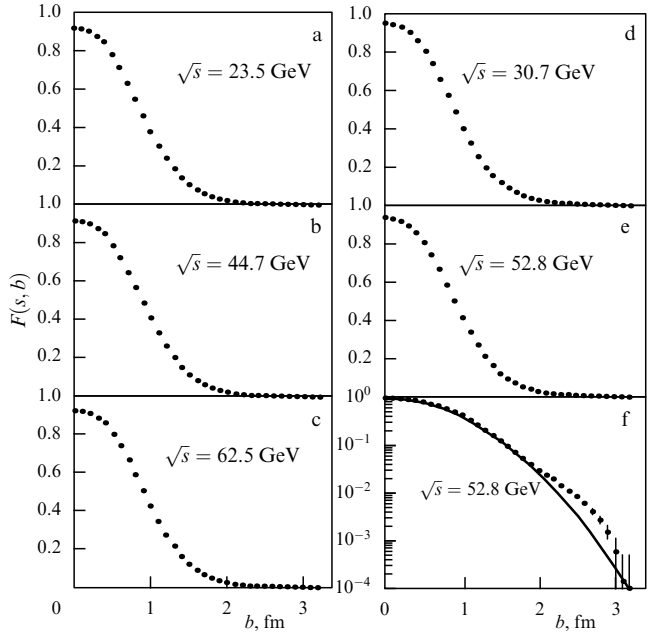

Figure 8. The overlap functions at ISR energies as functions of the impact parameter look similar (borrowed from [230]). The solid line at $\sqrt{s} = 52.8$ GeV is explained in the text.

approximations for the overlap function demonstrated in Fig. 6 have yet been proposed.

It is instructive to confront the shape of the overlap function $F(s,t)$ with results obtained in the impact parameter interpretation of proton–proton scattering. They were presented in Refs [229, 230] for ISR data and are demonstrated in Figs 7 and 8. The b-transformed amplitude $h(s,b)$, the overlap function $F(s,b)$, and the eikonal $\Omega(s,b)$ are shown in Fig. 7 at the energy $\sqrt{s} = 52.8$ GeV [229]. The transformed amplitude is almost Gaussian from the center to 2 fm with some flattening near the center. There is a tail beyond 2 fm with a much flatter slope. The flattening of the overlap function at the center is much stronger, while the eikonal is steeper there. Hence, we should not identify these three curves at small b, even though they almost coincide beyond 2 fm.

Similar features are seen in Fig. 8, taken from [230], where $F(s,b)$ at the same energy is displayed. The solid line on the logarithmic scale is a Gaussian adjusted to fit at $b = 0$ and $b = 1.6$ fm. A Gaussian adjusted between 0.6 and 1.6 fm would be higher at $b = 0$ and would require additional flattening. This flattening at small b corresponds directly to negative values of $F(s,t)$ at large $|t|$, as seen in Fig. 6. In the same way, slight variations of the eikonal $\Omega(s,b)$ at small b may lead to drastic disagreement of model fits with experimental data. Therefore, their success or failure at large $|t|$ depends on the accuracy of the chosen form of the eikonal at low b. A long tail above the solid line for large impact parameters is clearly seen in Fig. 8f. These figures demonstrate how accurate model formulas must be to correctly reproduce either the overlap function or the eikonal if the final goal is to describe the differential cross sections outside the diffraction peak.

A small 'edge' correction to the Gaussian shape of the eikonal has been claimed to be necessary for fits of experimental data at ISR energies on increasing total cross sections and structures of the differential cross sections in Refs [231–233]. For example, the correction factor k with some specific dependence on the impact parameter was introduced into the overlap function $F(s,b)$ in [233]. It changes the shape at small b and makes it similar to that shown in Fig. 7:

$$F(s,b) = P\exp\left(-\frac{b^2}{4B}\right) k\left(s, b\exp\left(-\frac{\gamma^2 b^2}{4B}\right)\right). \qquad (81)$$

It turns out that in the t-representation, the corresponding overlap function $F(s,t)$ has two zeros at $|t| = 0.645$ and 3.83 GeV^2 and becomes practically indistinguishable from zero already at $|t| > 3.5$ GeV^2. The last statement is in full agreement with the conclusions in Refs [59, 60].

Although the overlap functions in Fig. 8 look quite similar to each other, there is a slight difference, which was analyzed in [230, 233]. This difference reveals itself in a small increase at the level of 4% of the overlap function, with an energy increase at the impact parameters (radii) of about 1 fm, which implies the peripheral origin of this phenomenon. That was also discussed earlier [234]. Moreover, in Ref. [230], which deals with the direct analysis of experimental data at ISR, a shoulder of the overlap function at 2.3 fm was noticed. Its origin is unknown.

The overlap function in the b-representation is used in Ref. [235] to distinguish between the mechanisms of absorption and reflection with the help of the unitarity equation. In the latter case, the differential cross section at large momentum transfers is predicted to be 4 times larger.

The impact parameter picture used in almost all phenomenological models is very helpful for a qualitative

description of the process. But the forms of the eikonal in the b-representation turned out to be very approximate. In our opinion, their wide use in most papers dealing with extension to larger angles suffers from this deficiency. There are some arguments [88] that the eikonal approximation is only valid for sums of leading terms of the tower diagrams, but this is not correct in general. This is applicable to almost collinear processes only and does not properly take the separation due to transverse momenta into account. That is why quasi-eikonal models were developed where the intermediate states take inelastic diffraction processes into account, in addition to elastic ones. As a result, formulas like (39) and (40) were proposed. The eikonal does not properly reproduce the s-channel cuts of the scattering amplitude due to multiple scattering [236]. By itself, it does not guarantee precise unitarization. Moreover, the procedure of unitarity corrections is not well defined, because it can be implemented differently. The accuracy of unitarity relation (26) in the b-representation is not absolutely clear either, as discussed above, while its use is mandatory for interpretation of experimental data. That is why the model predictions shown in Fig. 2 fail to explain the data.

There is a drastic difference between the use of the Gaussian shape for the amplitude in the s-channel unitarity condition and the same shape for the overlap function, as well as its use directly in the b-representation. The exponential decrease [see Eqn (6)] of the differential cross section in the diffraction cone as a function of $|t|$ (or a Gaussian decrease with the angle) is an experimental observation. It can be used anywhere within its applicability range, as was done, for example, in solving Eqn (18). Hence, this solution is quite successful in fits of experimental data in the Orear region. The same shape cannot be used for the t-dependence of the overlap function, although it plays an important role in the formation of cone behavior.

It is often argued that the Fourier transform of the Gaussian is a Gaussian and therefore this shape can also be used in the b-representation. While the first part of the statement is correct, the second is wrong. The tails of differential cross sections are very sensitive to small b. Slight variations of this shape at small impact parameters lead to crucial changes in the behavior of the amplitude at large transferred momenta. Therefore, the predictions shown in Fig. 2, which use the impact parameter profiles close to Gaussian ones even in the vicinity of $b = 0$, are still successful inside the diffraction cone but completely fail outside it, where central collisions play an important role. It is very difficult in a particular model to guess the proper decline from the Gaussian shape at small impact parameters, which drastically influences the differential cross section at large transferred momenta.

Therefore, attempts to use non-Gaussian electromagnetic form factors were of some help in improving the situation, because they are closer in shape to the eikonal demonstrated in Figs 7 and 8. Further progress in this direction is necessary in order to understand the geometric content of the interaction region in ordinary space and time.

Nevertheless, it is hardly justified to blame the phenomenological model builders for their failure to predict the behavior of differential cross sections at large transferred momenta, where the differential cross section is many orders of magnitude lower than in the diffraction peak. The great and important task of fits of the energy behavior of total and elastic cross sections, the (s, t)-dependence of the differential cross section, and the ratio ρ in a wide range of energies and transferred momenta cannot be accomplished without free parameters and the physical intuition of model builders. The switch to higher energies allows eliminating corrections due to secondary Reggeons and improving the fits. There is hope of gaining clearer insight into the geometrical picture of hadron interactions.

4.2.5 Real part of the elastic scattering amplitude at nonzero transferred momenta. There are no reasonable arguments to neglect the t-dependence of the ratio $\rho(s, t)$ in (2) or of the phase ζ in (13): it seems to be important, even inside the diffraction cone. Using formula (10) and assuming that $\operatorname{Im} A(s, t)$ mainly determines the shape of the differential cross section in this region, we find that the real part must vanish at

$$t_0 = -2\,\frac{\mathrm{d}\ln\sigma_{\mathrm{t}}(s)/\mathrm{d}\ln s}{\mathrm{d}B(s)/\mathrm{d}\ln s}\,. \tag{82}$$

With the $\ln^2 s$-dependence of σ_{t} in (32) and $B(s)$ in (34) and using relation (42), we have

$$|t_0| = \frac{2}{B} = \frac{16\pi}{\sigma_{\mathrm{t}}}\,, \tag{83}$$

and hence $t_0 \to 0$ as $\sigma_{\mathrm{t}} \to \infty$. The estimates at LHC energies are $0.1 < |t| < 0.3\ \mathrm{GeV}^2$. Notably, they agree with the results obtained in the models in [165, 192].

There were several attempts to consider the behavior of $\rho(s, t)$ at larger transferred momenta in Refs [165, 230, 237–240]. The main efforts were spent on preventing differential cross sections from vanishing at those values of t where the imaginary part of the amplitude is zero in a particular model. The ratio $\rho(t)$ should be infinite, e.g., as in the models in Refs [165, 230]. The number of zeros of the imaginary part is sometimes greater than one. This is typical in the Fraunhofer diffraction or in models with electromagnetic form factors. Therefore, the singularities of $\rho(t)$ appear at different t in different models. The real part of the amplitude fills in these kinks, leaving some traces like shoulders or dips in the differential cross sections. For example, it is predicted in Ref. [165] that for pp scattering at 8 TeV, such traces appear at $|t| \approx 0.35\ \mathrm{GeV}^2$ and at $1.5\ \mathrm{GeV}^2$.

In Refs [237, 238], the dispersion relation between the phase and the modulus of the elastic amplitude considered in Refs [241, 242] was used with some input for the modulus fitted to the experimental data at laboratory energies above 100 GeV. The conclusion was that the real part exhibits a zero in the t-distribution above 200 GeV, which moves away from the forward direction as the energy increases.

In Ref. [239], the eikonal approximation was used following the proposal in Ref. [243]. Information about the interference region with a Coulomb amplitude similar to that in Eqn (30) was inserted into the total amplitude, with the result

$$\begin{aligned} A(s, t) = &-\frac{8\pi\alpha}{|t|}\, s f_1\bigl(|t|\bigr) f_2\bigl(|t|\bigr) \exp\bigl(\mathrm{i}\alpha\Phi\bigr) \\ &+ \mathrm{i}s\sigma_{\mathrm{t}} \exp\left(\frac{Bt}{2} - \mathrm{i}\zeta(s, t)\right)\left\{1 - \mathrm{i}\alpha\int_{-\infty}^{0} \mathrm{d}t'\, \ln\frac{t'}{t}\right. \\ &\left.\times\,\frac{\mathrm{d}}{\mathrm{d}t'}\left(f_1\bigl(|t'|\bigr) f_2\bigl(|t'|\bigr) \exp\left[\frac{Bt'}{2} - \mathrm{i}\bigl(\zeta(s, t') - \zeta(s, 0)\bigr)\right]\right)\right\}. \end{aligned} \tag{84}$$

The t-dependence of the phase was parameterized with the help of five parameters as

$$\zeta(t) = \zeta_0 + \zeta_1\left(\frac{t}{t_0}\right)^{\kappa} \exp\left(v|t|\right) + \zeta_2\left(\frac{t}{t_0}\right)^{\lambda}, \quad t_0 = -1 \text{ GeV}^2 . \tag{85}$$

The results showed that the phase [related to ρ by (14)] increases from values close to zero at $t = 0$ to about 0.5 in the interval $0.5 < |t| < 1$ GeV^2. This conclusion disagrees with the results in Refs [73, 74, 165] as well as with the arguments presented below.

A more general approach using the s-channel unitarity condition was developed in Ref. [240]. As explained above, the integral equation for the elastic amplitude is valid in the Orear region. Its analytic solution (77) was first obtained in the approximation where the values of ρ in f_ρ were replaced by their average values in the diffraction cone and in the Orear region. No zeros of the imaginary part of the amplitude were obtained. The dips at 7 TeV and lower energies were explained as resulting from damped oscillations. The necessity to introduce large negative values of ρ into the Orear region is the main outcome and surprise of the fit in Ref. [60]. In principle, this could happen if there were zeros of the imaginary part of the amplitude in this region, which would require very large values of $|\rho|$ near them. But there seem to be no such zeros there. We discuss this problem in more detail.

We first recall asymptotic predictions. It was shown in [244] that the ratio of real to imaginary parts of the amplitude can be calculated asymptotically at nonzero transferred momenta t as

$$\rho = \rho_0\left[1 + \frac{\tau\left(\mathrm{d}f(\tau)/\mathrm{d}\tau\right)}{f(\tau)}\right]. \tag{86}$$

We consider the leading term of solution (77). With the imaginary part of the amplitude in the Orear region represented as

$$\operatorname{Im} A(s,t) = C_0(s) f(\tau) , \tag{87}$$

it is possible to calculate ρ.

The very first approximation was to use the first term of solution (77) with average values of ρ both in the diffraction peak ($\rho_\mathrm{d} \approx \rho_0$) and in the Orear region (ρ_l) [240]. Then the following behavior of ρ was obtained:

$$\rho(s,t) = \rho_0\left(1 - \frac{a\sqrt{|t|}}{2}\right), \tag{88}$$

where

$$a = \sqrt{2B \ln \frac{Z}{1 + \rho_0\,\rho_\mathrm{l}}} . \tag{89}$$

We note that ρ passes through zero and changes sign at $|t| = 4/a^2 \approx 0.1$ GeV^2. This agrees with the general theorem on the change of sign of the real part of the high-energy scattering amplitude, which was first proved in Ref. [84]. A similar effect is discussed in Ref. [165]. But it is difficult to obtain $\rho_\mathrm{l} = -2.1$ as an average of (88) over the Orear region.

Moreover, this behavior of an unbounded decrease in ρ with $|t|$ does not look satisfactory. It can in fact be damped if instead of replacing ρ by ρ_l in the solution, we differentiate f

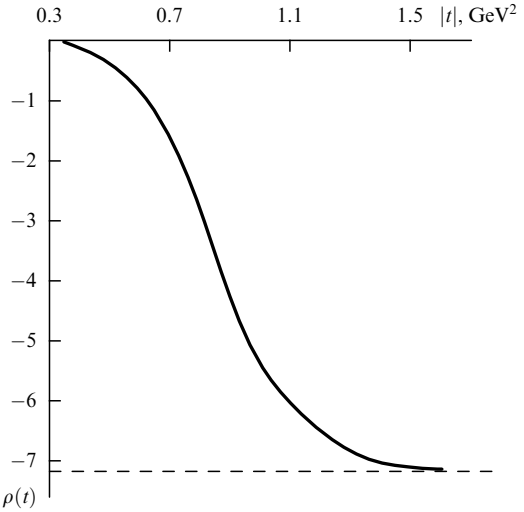

Figure 9. The ratio of the real to imaginary part of the amplitude obtained from the solution of Eqn (90) that follows from the unitarity condition [240].

according to (86), inserting there Eqn (87), i.e., the first term in (77). The following differential equation is then obtained:

$$\frac{\mathrm{d}v}{\mathrm{d}x} = -\frac{v}{x} - \frac{2}{x^2}\left[\frac{Z\exp\left(-v^2\right) - 1}{\rho_0^2} - 1\right]. \tag{90}$$

Here, $x = \sqrt{2B|t|}$ and $v = \sqrt{\ln\left(Z/f_\rho\right)}$. The dependence $\rho(t) = \left(Z\exp\left(-v^2\right) - 1\right)/\rho_0$ is shown in Fig. 9. It has a single zero at $|t| \approx 0.3$ GeV^2 and, which is indeed impressive, a large negative saturation value $\rho(|t| \to \infty) = -1/\rho_0$ for high transferred momenta $|t|$. We note that f_ρ tends to zero there. In the Orear region $0.3 < |t| < 1.4$ GeV^2, $\rho(t)$ steeply decreases. Nevertheless, taking the $\sqrt{|t|}$-exponential decrease in the distribution into account, the estimate of its average value -2.1 in this interval is not very bad at all, especially if we consider the result shown in Fig. 9 as another extreme approximation compared to Eqn (88).

The bold use of this procedure for derivation of Eqn (90) with $\rho(t)$ inserted directly into the solution is nevertheless not satisfactory, either. The two possibilities above should be regarded as two extremes for the shapes of $\rho(t)$.

Strictly speaking, the behavior of $\rho(t)$ should be taken into account primarily in the integrand. Then, inserting expression (86) in place of ρ_l in Eqn (76) and integrating by parts, we derive the linear integral equation

$$\operatorname{Im} A(x) = \frac{1}{Z\sqrt{\pi}}\int_{-\infty}^{+\infty} \mathrm{d}y \exp\left[-(x-y)^2\right] + \left[1 + 0.5\rho_0^2 + \rho_0^2(y-x)y\right] \operatorname{Im} A(y) , \tag{91}$$

with $F(p,\theta) = 0$ and new variables $x = \sqrt{B/2}\,p\theta$ and $y = \sqrt{B/2}\,p\theta_1$. The kernel of this equation is not symmetric. Its solution has not yet been obtained, even numerically. However, some preliminary asymptotic estimates can be obtained from it [240].

In the preasymptotic energy region, we obtained [58] the Orear regime $\operatorname{Im} A \propto \exp\left(-ap\theta\right) \approx \exp\left(-ap_\mathrm{t}\right)$ with the exponential fall-off of the amplitude as a function of angles. We therefore seek a solution of Eqn (91) in the form $\operatorname{Im} A(x) = \exp\left(-ax\sqrt{2/B}\,\right)\phi(x)$. The Gaussian exponential

shifts to $x - y - a/\sqrt{2B}$. Replacing it with the δ-function of this argument, we obtain the equation in finite differences:

$$\phi(x) = Z^{-1} \exp\left(\frac{a^2}{2B}\right)\left[1 + 0.5\rho_0^2\left(1 + \frac{a^2}{B} - ap_t\right)\right] \times \phi\left(x - \frac{a}{\sqrt{2B}}\right). \quad (92)$$

Again, we cannot solve it directly, but reach an important conclusion about the zeros of the imaginary part of the amplitude. The expression in the square brackets is equal to zero at

$$p_{t0} = \frac{2}{a\rho_0^2}\left[1 + 0.5\rho_0^2\left(1 + \frac{a^2}{B}\right)\right] \approx \frac{2}{a\rho_0^2}. \quad (93)$$

With the present-day values of B, a, and ρ_0^2, this zero would appear at an extremely large $p_{t0} \approx 20$ GeV. However, zeros of the imaginary part of the amplitude in the Orear region just above the diffraction cone might appear as zeros of $\phi(x)$ itself. This result does not contradict the above statement about the absence of zeros in the case of small oscillatory terms in the solution of a homogeneous linear integral equation.

Moreover, the equation tells us that $\phi(x)$ and, consequently, the imaginary part of the amplitude can have zeros at $x_n = x_0 + a/\sqrt{2B}$. On the p_t axis, these zeros would be placed at rather short distances from one another.

In the black-disk limit, Z tends to 0.5. If ρ loses in the competition with $\ln(Z/f_\rho)$ and the argument of the logarithm becomes extremely close to 1 or even less, that would mean a drastic change of the regime in the Orear region [245]. What the outcome of the competition between decreasing Z and the negative values of ρ will be poses an interesting problem. Experimental data at higher energies will be able to give the answer.

As we see, the real part of the amplitude can dominate at large transferred momenta according to the unitarity condition. Compared to the imaginary part, it can be large and negative there. This conclusion contradicts, for example, the results of the models in [92, 165] with electromagnetic form factors, where the dominance of the imaginary part, on the contrary, is claimed everywhere except the tiny regions near its zeros placed in the Orear region, in particular. This disagrees with the above results. We must remember, however, that ρ is infinite at these zeros (see Fig. 10). A similar behavior of ρ in the case of a single zero was predicted in Ref. [230] at ISR energies, as shown in Fig. 10.

A similar shape of ρ is obtained in Ref. [165] at $|t| \approx 1.5$ GeV^2, but for the energy $\sqrt{s} = 8$ TeV. The real part decreases with $|t|$. Thus, the conclusions in different papers about the behavior of the real and imaginary parts of the elastic scattering amplitude are contradictory and require further theoretical studies and new experimental data.

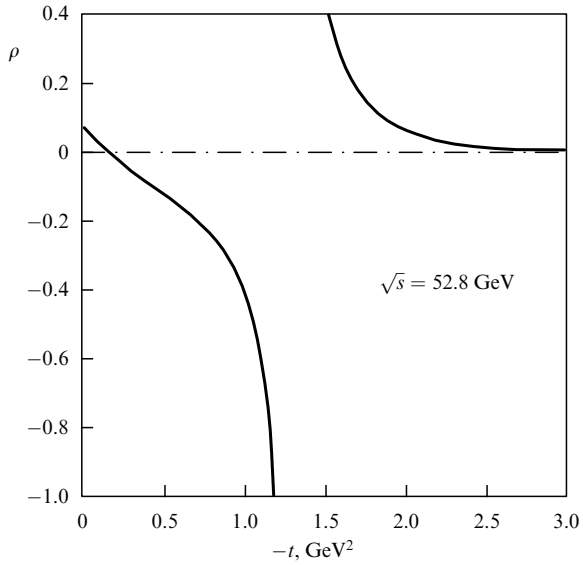

Figure 10. The dependence of the ratio of the real part to the imaginary part of the amplitude on transferred momenta obtained in a certain phenomenological fit [230] of experimental data at $\sqrt{s} = 52.8$ GeV. The singularities indicate the position where the imaginary part vanishes.

4.3 Scaling laws

We have written two formulas, (10) and (86), for the same function $\rho(s,t)$. Therefore, these two expressions must be identical. Equating them, we obtain [246] the partial differential equation

$$p - f(x)q = 1 + f(x), \quad (94)$$

where $p = \partial u/\partial x$, $q = \partial u/\partial y$, $u = \ln \operatorname{Im} A(s,t)$, $f(x) = 2\rho(s,0)/\pi$, $x = \ln s$, and $y = \ln|t|$. As usual, the variables s and $|t|$ should be regarded as scaled by the corresponding constant factors s_0^{-1} and $|t_0|^{-1}$.

Equation (94) can be rewritten as

$$\frac{\partial u}{\partial \ln \sigma_t} - \frac{\partial u}{\partial \ln t} = 1 + \frac{d \ln s}{d \ln \sigma_t}.$$

In the asymptotic black-disk limit $\sigma_t \propto \ln^2 s$ and $\rho(s,0) = \pi/\ln s$, we obtain

$$xp - 2q = x + 2, \quad (95)$$

and the solution is

$$u = \varphi_1\left(x \exp\frac{y}{2}\right) + x - y. \quad (96)$$

This yields the scaling law for

$$\frac{|t|}{s} \operatorname{Im} A(s,t) = \exp\left[\varphi_1\left(\sqrt{|t|}\ln s\right)\right] = \phi(z_1), \quad (97)$$

which implies a universal scaling dependence on a single variable $z_1 = \sqrt{|t|}\ln s$.

We temporarily neglect the contribution of the real part of the amplitude to the differential cross section. Then the asymptotic scaling law for the differential cross section times t^2 should be

$$t^2 \frac{d\sigma}{dt} = \phi_1^2\left(\sqrt{|t|}\ln s\right). \quad (98)$$

We note that the additional t^2-factor can be replaced by an s-dependence if absorbed in the argument of the scaling function ϕ. Then this formula coincides with that obtained in the geometric scaling approach [145, 247]. Thus, we have proved that the solution of partial differential equation (94) with the properly chosen $f(x)$ leads to the results known previously from geometric scaling.

At the same time, Eqn (94) is more general and can be used for different assumptions about $f(x)$. In particular, the

behavior of the total cross section at present energies is often approximated by formula (67) as a sum of a large constant term and another term that increases as some power of energy (see [192] for a recent reference). In this case, $\rho(s,0) = \pi\Delta/2$, and the equation is

$$p - \Delta q = 1 + \Delta\,. \tag{99}$$

Its solution is

$$u = \varphi_2(\Delta x + y) + x - y\,. \tag{100}$$

From here, we obtain another universal scaling dependence of the differential cross section on a single variable $z_2 = |t|s^{\Delta}$,

$$t^2\,\frac{\mathrm{d}\sigma}{\mathrm{d}t} = \phi_2^2\left(|t|s^{\Delta}\right), \tag{101}$$

which could be valid at preasymptotic energies.

It follows from the above expressions that the energy dependence of the scaling variable is determined by the behavior of the total cross section, $|t|\sigma_{\mathrm{t}}$, if only the first term in Eqn (9) is used. If this scaling were valid, one would be able to predict the shape of the differential cross section at a higher energy once the total cross section is known there. The preliminary results of work with experimental data at energies from ISR to LHC have shown that just this dependence best reproduces the similarity of the shapes of the corresponding lines, even though their normalization differs somewhat. Further studies are necessary.

The above scaling laws must be satisfied for the imaginary part of the amplitude times the factor $|t|/s$ (see (97)). It follows from Eqn (10) that the real part satisfies an analogous scaling law, albeit with another factor, which differs in the two cases considered above. This would lead to the scaling violating terms when the contribution of the real part of the amplitude to the differential cross section is taken into account. The above scaling dependences of the differential cross section are modified as

$$t^2\,\frac{\mathrm{d}\sigma}{\mathrm{d}t} = \phi_1^2(z_1) + 0.25\pi^2|t|\phi_1'^2(z_1)\,, \tag{102}$$

$$t^2\,\frac{\mathrm{d}\sigma}{\mathrm{d}t} = \phi_2^2(z_2) + 0.25\pi^2\Delta^2 z_2^2\phi_2'^2(z_2)\,. \tag{103}$$

The violation of scaling laws is different in these cases. The first law acquires a term with the coefficient depending only on the transferred momentum, while the second law acquires a term with the coefficient that depends both on energy and on the transferred momentum.

This violation of scaling laws must be negligible in the diffraction cone because the squared ratio of the real part to the imaginary part — which is crucial for the differential cross section — is extremely small there. It would be interesting to learn about the effect of these terms outside the cone, especially in the Orear region of transferred momenta.

We note that at small values of their arguments z_i, the scaling functions $\phi_i(z_i)$ must be respectively proportional to z_1^2 and to z_2, for the differential cross section to be equal to a constant at $t = 0$.

4.4 Hard scattering at large angles

4.4.1 Dimensional counting. The energy dependence of high-energy scattering processes at a fixed center-of-mass angle is of special interest. Dimensional scaling laws have been developed as an approach to understanding it. The large-angle scattering is determined by contributions due to central interactions of internal domains inside the colliding particles. The estimates according to perturbative QCD become justified due to the asymptotic freedom property. They depend on the number of constituent fields of the hadrons [248–250]. At large s and t and a fixed ratio s/t, we have

$$\left.\frac{\mathrm{d}\sigma}{\mathrm{d}t}\right|_{\mathrm{AB}\to\mathrm{CD}} \propto s^{-n+2} f\left(\frac{t}{s}\right), \tag{104}$$

where n is the total number of fields in A, B, C, D that carry a finite fraction of the momentum.

Assuming the existence of quark constituents, the $s \to \infty$, fixed-t/s prediction for pp scattering [249, 250] is $\mathrm{d}\sigma/\mathrm{d}t \propto s^{-10}$. For the elastic amplitude, it is

$$A_1(s,t) \propto \left(\frac{s_0}{s}\right)^{n/2-2} f_1\left(\frac{s}{t}\right). \tag{105}$$

This form can become more complicated for multiple scatterings. For example, the lowest-order graphs for m rescatterings [251] behave as

$$A_m(s,t) \propto \left(\frac{s_0}{s}\right)^{(n-m+1)/2-2} f_m\left(\frac{s}{t}\right), \tag{106}$$

and could become the leading ones. However, due to higher-order corrections, the resulting behavior could change not so drastically, and the result would be close to the initial estimate (105), as is shown in Ref. [252]. Further progress beyond the simple quark-counting rules was slowed down by complications in calculating the enormous number of Feynman diagrams.

4.4.2 Coherent scattering. In parallel, there were attempts to explain the $|t|^{-8}$ regime in pp scattering by dynamical mechanisms with the help of simple Feynman graphs. For protons (or their subregions) consisting of three valence quarks, we can assume coherent exchange by gluons [253–255] or by color-neutral pairs of gluons [256, 257] between them. The propagators of three gluons and their couplings produce an $\alpha_{\mathrm{s}}^6|t|^{-6}$ dependence, and two powers in the denominator are added by kinematical factors. The general problem of these approaches is the necessity to introduce additional factors in order to preserve both protons in their initial states in large-angle scattering. The corresponding powers of the QCD coupling constant should be included, of course, which leads to possible (strong?) modifications of the simple power law. Also, the exchange by three Pomerons instead of three pairs of gluons is possible. Because three colliding quarks share the total energy of the proton equally, their shares are smaller, and the whole process is farther from the asymptotic regime if treated at the parton level. None of these questions have been quantitatively resolved yet.

We note that the large-$|t|$ behavior of Reggeons composed of two Reggeized partons (quarks, gluons) can be calculated from the BFKL equation [258, 259].

The multi-Pomeron exchange for hadrons in a state with a minimum number of partons was considered in [260]. It was concluded that the differential cross section factors as a product of two $|S_0(s)|^2$, representing the probability of finding the initial and final particles in a 'bare' state, and

$d\hat{\sigma}(s,t)/dt$, describing the hard exchange interaction:

$$\frac{d\sigma}{dt} = \left|S_0(s)\right|^2 \frac{d\hat{\sigma}(s,t)}{dt} . \qquad (107)$$

The first factor describes the contribution of large transverse distances and the second represents the contribution of small ones. The hard exchange is determined by the Pomeron vertices, which are known semiclassically:

$$\frac{d\hat{\sigma}(s,t)}{dt} \propto g_1^2(t)\, g_2^2(t) \propto \frac{\left(\alpha_s(t)\right)^v}{|t|^N} \qquad (108)$$

with

$$v = n_1 + n_2 + |n_1 - n_2| ,$$
$$N = 0.5\left[3(n_1 + n_2) + |n_1 - n_2| - 1\right] , \qquad (109)$$

where n_i are the numbers of valence quarks in the colliding hadrons. This leads to a $|t|^{-8}$ behavior for pp and $|t|^{-7}$ for πp. The quantitative comparison with experimental data is more difficult because of much smaller values of the differential cross sections in this region and, correspondingly, larger error bars.

5. Discussion and conclusions

The new experimental data of the TOTEM collaboration at the LHC about elastic scattering of protons at an energy of 7 TeV has revived interest in these processes. The picture of very short-wavelength hadron collisions has become available, adding to our insight into the spatial structure of colliding particles and providing new intrinsic information pertaining to very short distance interactions. The total and elastic cross sections show a stable increase with energy. The share of elastic processes increases. The differential cross section has very intriguing properties. The exponential $|t|$-decrease persists at small transferred momenta, analogously to lower-energy data. But the diffraction cone slope is larger compared with low energies; it is stable up to transferred momenta $|t| \approx 0.3$ GeV^2, then this peak steepens and a dip appears at $|t| \approx 0.53$ GeV^2, with a subsequent maximum at $|t| \approx 0.7$ GeV^2. At somewhat larger angles, the exponential in the $\sqrt{|t|}$-regime prevails. It is replaced by the $|t|^{-8}$ behavior at ever larger transferred momenta, $|t| > 2$ GeV^2. At the same time, we are waiting for measurements at extremely small angles in the interference region of Coulomb and nuclear amplitudes to gain some knowledge about the real part of the forward scattering amplitude. It would be extremely interesting to learn its energy behavior and check our predictions from the dispersion relations.

The steeper slopes of the diffraction peak and of the Orear region at higher energies, and, correspondingly, their smaller extensions clearly demonstrate that it becomes more and more difficult for a high-energy particle to preserve its identity when scattering at larger transverse momenta.

This increase in the total cross section and, especially, in the share of the elastic cross section, as well as the peculiar change of regimes in the $|t|$-behavior of the differential cross section, require a theoretical interpretation. Short of a complete theory of hadron dynamics, we have to turn our attention to phenomenological models and some rare rigorous theoretical relations. The region of large transferred momenta became an Occam razor for them, as explained above.

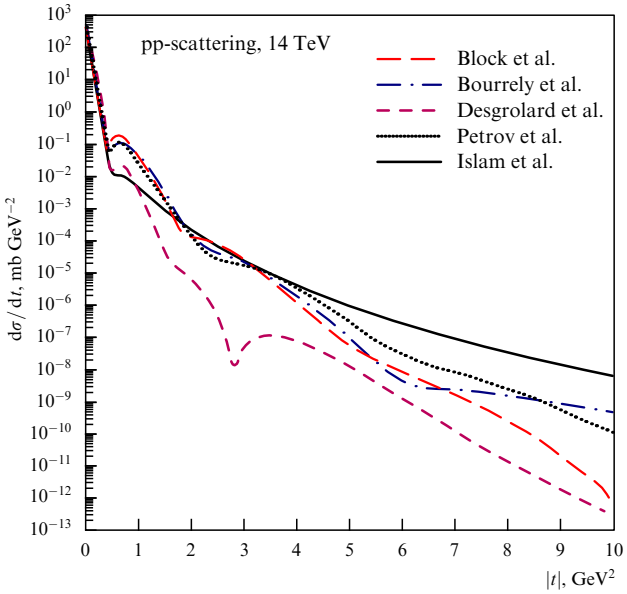

Figure 11. Model predictions for the behavior of the differential cross section of proton–proton scattering at $\sqrt{s} = 14$ TeV, presented in Ref. [119].

The geometric picture of the internal structure of protons and their collisions requires larger disk radii increasing with energy. Their blackness increases as well. Some separate subregions of different sizes and opacity are considered. The impact parameter approach is decisive in deciphering this structure. At ISR energies, the increase in the total cross section was attributed to some peripheral regions of nucleons. It is important to juxtapose these findings with the LHC data. The approach to the black-disk asymptotic limit has become very interesting. The proposal of geometric scaling reducing the number of independent variables is under investigation. At the same time, the scaling law may happen to be different from the geometric scaling.

There are many phenomenological models at our disposal, but it is still difficult to choose any particular one among them. Most of them are quite successful, albeit with many adjustable parameters, in describing the energy behavior of the cross sections and the main bulk of the elastic processes in the diffraction cone, but fail in their predictions outside it. The dynamical origin of many assumptions is still missing. The small details of the suspected break at small t, of the steepened slope, and of possible weak oscillations over a smooth exponential behavior of the diffraction peak are under investigation.

There are predictions of several dips and/or visible oscillatory behavior imposed on the trend of a generally decreasing dependence on the transferred momentum. As an example, in Fig. 11 borrowed from [119], the results of some model predictions for the differential cross section of proton–proton scattering at $\sqrt{s} = 14$ TeV are shown up to quite high values $|t| = 10$ GeV^2. They differ significantly, and further accurate experimental data expected to be obtained in 2015 – 2016 will surely be decisive in the choice of a model (if any!). The experience with unsuccessful predictions at 7 TeV in the region outside the diffraction cone is not very encouraging.

The problem of the behavior of the real part of the elastic scattering amplitude at nonforward transferred momenta is becoming very important. While the imaginary part of the

amplitude dominates at small angles in the diffraction cone, there are indications that just the real part prevails at high transferred momenta. The unitarity condition indicates some ways to solve this problem. However, there are other approaches with different conclusions.

Another important unsolved problem is the behavior of the overlap function. It certainly dominates in the diffraction cone, but seems to become negligibly small outside it. The phases of matrix elements of inelastic processes must play an important role in attempts to recover its shape. However, this presents the extremely difficult theoretical task of modeling them.

Unfortunately, there is little progress in understanding the regime of power counting for very hard constituent parton scattering, even though some recent attempts are quite promising.

To conclude, the aforementioned list of problems is not at all complete. Many other details should be clarified. Further experimental data will definitely shed light on ways to resolve them.

Acknowledgements

This work was supported by the RFBR grant 12-02-91504-CERN-a and by the RAS–CERN program.

References

1. Foley K J et al. *Phys. Rev. Lett.* **11** 425 (1963); *Phys. Rev. Lett.* **11** 503 (1963)
2. Cocconi G et al. *Phys. Rev. Lett.* **11** 499 (1963)
3. Krisch A D *Phys. Rev. Lett.* **11** 217 (1963)
4. Narayan D S, Sarma K V L *Phys. Lett.* **5** 365 (1963)
5. Orear J *Phys. Rev. Lett.* **12** 112 (1964)
6. Orear J *Phys. Lett.* **13** 190 (1964)
7. Baker W F et al. *Phys. Rev. Lett.* **12** 132 (1964)
8. Cocconi G et al. *Phys. Rev.* **138** B165 (1965)
9. Orear J et al. *Phys. Rev.* **152** 1162 (1966)
10. Allaby J V et al. *Phys. Lett. B* **27** 49 (1968)
11. Allaby J V et al. *Phys. Lett. B* **28** 67 (1968)
12. Akerlof C W et al. *Phys. Rev. D* **14** 2864 (1976)
13. Ayres D S et al. *Phys. Rev. D* **15** 3105 (1977)
14. Asa'd Z et al. *Nucl. Phys. B* **255** 273 (1985)
15. Amaldi U et al. *Phys. Lett. B* **44** 112 (1973)
16. Amendolia S R et al. *Phys. Lett. B* **44** 119 (1973)
17. Böhm A et al. *Phys. Lett. B* **49** 491 (1974)
18. Kwak N et al. *Phys. Lett. B* **58** 233 (1975)
19. Albrow M G et al. *Nucl. Phys. B* **108** 1 (1976)
20. Hartmann J L et al. *Phys. Rev. Lett.* **39** 975 (1977)
21. Conetti S et al. *Phys. Rev. Lett.* **41** 924 (1978)
22. Baksay L et al. *Nucl. Phys. B* **141** 1 (1978)
23. Nagy E et al. *Nucl. Phys. B* **150** 221 (1979)
24. Amaldi U, Schubert K R *Nucl. Phys. B* **166** 301 (1980)
25. Kuznetsov A A et al. *Sov. J. Nucl. Phys.* **33** 74 (1981) [*Yad. Fiz.* **33** 142 (1981)]
26. Schiz A et al. *Phys. Rev. D* **24** 26 (1981)
27. Fidecaro G et al. *Phys. Lett. B* **105** 309 (1981)
28. Faissler W et al. *Phys. Rev. D* **23** 33 (1981)
29. Rubinstein R et al. *Phys. Rev. D* **30** 1413 (1984)
30. Breakstone A et al. *Nucl. Phys. B* **248** 253 (1984)
31. Eisenhandler E et al. *Nucl. Phys. B* **113** 1 (1976)
32. Favart D et al. *Phys. Rev. Lett.* **47** 1191 (1981)
33. Amos N et al. *Nucl. Phys. B* **262** 689 (1985)
34. Amos N A et al. *Phys. Lett. B* **247** 127 (1990)
35. Ambrosio M et al. *Phys. Lett. B* **115** 495 (1982)
36. Sakamoto S et al. *Nucl. Phys. B* **195** 1 (1982)
37. Bozzo M et al. *Phys. Lett. B* **147** 385 (1984)
38. Bozzo M et al. *Phys. Lett. B* **155** 197 (1985)
39. Breakstone A et al. *Phys. Rev. Lett.* **54** 2180 (1985)
40. Bernard D et al. *Phys. Lett. B* **171** 142 (1986)
41. Bernard D et al. *Phys. Lett. B* **198** 583 (1987)
42. Augier C et al. *Phys. Lett. B* **316** 448 (1993)
43. Abe F et al. *Phys. Rev. D* **50** 5518 (1994)
44. Abazov V M et al. (D0 Collab.) *Phys. Rev. D* **86** 012009 (2012); arXiv:1206.0687
45. Zotov N P, Rusakov S V, Tsarev V A *Sov. J. Part. Nucl.* **11** 462 (1980) [*Fiz. Elem. Chastits At. Yadra* **11** 1160 (1980)]
46. Amaldi U, arXiv:1206.3954
47. Dataset of differential elastic cross sections, http://www.theo.phys.ulg.ac.be/~cudell/data/
48. Antchev G et al. (TOTEM Collab.) *Europhys. Lett.* **95** 41001 (2011)
49. Antchev G et al. (TOTEM Collab.) *Europhys. Lett.* **96** 21002 (2011)
50. Cheng H, Wu T T *Phys. Rev. D* **1** 1069 (1970); *Phys. Rev. D* **1** 1083 (1970)
51. Gribov V N, Migdal A A *Sov. J. Nucl. Phys.* **8** 583 (1969) [*Yad. Fiz.* **8** 1002 (1968)]
52. Bronzan J B, Kane G L, Sukhatme U P *Phys. Lett. B* **49** 272 (1974)
53. Fischer J, Kolář P *Phys. Lett. B* **64** 45 (1976)
54. Fischer J, Kolář P *Phys. Rev. D* **17** 2168 (1978)
55. MacDowell S W, Martin A *Phys. Rev.* **135** B960 (1964)
56. Van Hove L *Nuovo Cimento* **28** 798 (1963)
57. Andreev I V, Dremin I M *JETP Lett.* **6** 262 (1967) [*Pis'ma Zh. Eksp. Teor. Fiz.* **6** 810 (1967)]
58. Andreev I V, Dremin I M *Sov. J. Nucl. Phys.* **8** 473 (1968) [*Yad. Fiz.* **8** 814 (1968)]
59. Andreev I V, Dremin I M, Gramenitskii I M *Nucl. Phys. B* **10** 137 (1969)
60. Dremin I M, Nechitailo V A *Phys. Rev. D* **85** 074009 (2012)
61. Adachi T, Kotani T *Prog. Theor. Phys.* **35** 485 (1966)
62. Adachi T, Kotani T *Prog. Theor. Phys.* **39** 785 (1968)
63. Islam M M *Nucl. Phys. B* **104** 511 (1976)
64. Kundrát V, Lokajíček M, Krupa D *Phys. Lett. B* **544** 132 (2002)
65. Kundrát V, Kašpar J, Lokajíček M, arXiv:0912.1188
66. Bethe H A *Ann. Physics* **3** 190 (1958)
67. Rix J, Thaler R M *Phys. Rev.* **152** 1357 (1966)
68. West G B, Yennie D R *Phys. Rev.* **172** 1413 (1968)
69. Solov'ev L D *JETP* **22** 205 (1966) [*Zh. Eksp. Teor. Fiz.* **49** 292 (1965)]
70. Locher M P *Nucl. Phys. B* **2** 525 (1967)
71. West G B, Yennie D R *Phys. Rev.* **172** 1413 (1968)
72. Cahn R *Z. Phys. C* **15** 253 (1982)
73. Selyugin O V *Phys. Lett. B* **333** 245 (1994)
74. Selyugin O V *Phys. Rev. D* **60** 074028 (1999); arXiv:1201.4458
75. Block M M *Phys. Rev. D* **54** 4337 (1996)
76. Block M M *Phys. Rep.* **436** 71 (2006)
77. Kundrát V, Lokajíček M *Z. Phys. C* **63** 619 (1994)
78. Desgrolard P, Jenkovszky L, Struminsky B *Eur. Phys. J. C* **11** 145 (1999)
79. Petrov V A, Predazzi E, Prokudin A *Eur. Phys. J. C* **28** 525 (2003)
80. Kopeliovich B Z et al. *Phys. Rev. Lett.* **85** 507 (2000)
81. Kopeliovich B Z et al. *Phys. Rev. D* **63** 054001 (2001)
82. Froissart M *Phys. Rev.* **123** 1053 (1961)
83. Martin A *Nuovo Cimento A* **42** 930 (1966)
84. Martin A *Phys. Rev. D* **80** 065013 (2009)
85. Azimov Ya I *Phys. Rev. D* **84** 056012 (2011); arXiv:1204.0984; arXiv:1208.4304
86. Heisenberg W *Z. Phys.* **133** 65 (1952)
87. Cheng H, Wu T T *Phys. Rev. Lett.* **24** 1456 (1970)
88. Cheng H, Wu T T *Phys. Lett. B* **34** 647 (1971)
89. Block M M, Cahn R N *Rev. Mod. Phys.* **57** 563 (1985)
90. Kinoshita T *Phys. Rev. D* **2** 2346 (1970)
91. Chou T T, Yang C N *Phys. Lett. B* **128** 457 (1983)
92. Bourrely C, Soffer J, Wu T T *Eur. Phys. J. C* **28** 97 (2003)
93. Islam M M, Luddy R J, Prokudin A V *Phys. Lett. B* **605** 115 (2005)
94. Islam M M, Luddy R J, Prokudin A V *Int. J. Mod. Phys. A* **21** 1 (2006)
95. Desgrolard P et al. *Eur. Phys. J. C* **16** 499 (2000)
96. Golec-Biernat K, Wüsthoff M *Phys. Rev. D* **60** 114023 (1999)
97. Petrov V A, Prokudin A V *Eur. Phys. J. C* **23** 135 (2002)
98. Donnachie A, Landshoff P V *Nucl. Phys. B* **244** 322 (1984)
99. Block M M et al. *Phys. Rev. D* **60** 054024 (1999)
100. Kovner A, Wiedemann U A *Phys. Rev. D* **66** 034031 (2002)
101. Troshin S M, Tyurin N E *Phys. Lett. B* **707** 558 (2012); arXiv:1111.4454
102. Merino C, Shabelski Yu M, arXiv:1204.0769

103. Chao A W, Yang C N *Phys. Rev. D* **8** 2063 (1973)
104. Amos N A et al. *Phys. Lett. B* **247** 127 (1990)
105. Cheng H, Walker J K, Wu T T *Phys. Rev. D* **9** 749 (1974)
106. Fagundes D A, Menon M J, Silva P V R G, arXiv:1208.3456
107. Abreu P et al. (Pierre Auger Collab.), arXiv:1107.4804
108. Block M M, Halzen F *Phys. Rev. D* **72** 036006 (2005)
109. Block M M, Halzen F *Phys. Rev. D* **73** 054022 (2006)
110. Block M M, Halzen F *Phys. Rev. D* **83** 077901 (2011); arXiv: 1205.5514; arXiv:1208.4086
111. Grau A et al. *Phys. Lett. B* **714** 70 (2012)
112. Okorokov V A, arXiv:0907.0951
113. Campos S D, Okorokov V A *Int. J. Mod. Phys. A* **25** 5333 (2010)
114. Fagundes D A, Menon M J *Nucl. Phys. A* **880** 1 (2012); arXiv: 1208.0510
115. Dremin I M, Nazirov M T *JETP Lett.* **37** 198 (1983) [*Pis'ma Zh. Eksp. Teor. Fiz.* **37** 163 (1983)]
116. Henzi R, Valin P *Phys. Lett. B* **132** 443 (1983)
117. Dremin I M, Nechitailo V A *Phys. Rev. D* **70** 034005 (2004)
118. Dremin I M, Nechitailo V A *Phys. Rev. D* **84** 034026 (2011)
119. Islam M M, Kašpar J, Luddy R J *Mod. Phys. Lett. A* **24** 485 (2009)
120. Jenkovsky L, Lengyel A, Lontkovskyi D *Int. J. Mod. Phys. A* (2012), in press
121. Dremin I M, Chernavskii D S *Sov. Phys. JETP* **11** 167 (1960) [*Zh. Eksp. Teor. Fiz.* **38** 229 (1960)]
122. Amati D, Cini M, Stanghellini A *Nuovo Cimento 10* **30** 193 (1963)
123. Akimov V N et al. *Nucl. Phys. B* **14** 285 (1969)
124. Dremin I M, Dunaevskii A M *Phys. Rep.* **18** 159 (1975)
125. Fukuda H, Iso C *Nuovo Cimento A* **43** 43 (1966)
126. Zalewski K, Van Hove L *Nuovo Cimento A* **46** 806 (1966)
127. Michejda L *Nucl. Phys. B* **4** 113 (1967)
128. Giffon M, Hama Y, Predazzi E *Z. Phys. C* **19** 311 (1983)
129. Sopkovich N J *Nuovo Cimento* **26** 186 (1962)
130. Dar A et al. *Phys. Rev. Lett.* **12** 82 (1964)
131. Durand L (III), Chiu Y T *Phys. Rev. Lett.* **12** 399 (1964)
132. Arnold R C *Phys. Rev.* **136** B1388 (1964)
133. Jackson J D *Rev. Mod. Phys.* **37** 484 (1965)
134. Wu T T, Yang C N *Phys. Rev.* **137** B708 (1965)
135. Byers N, Yang C N *Phys. Rev.* **142** 976 (1966)
136. Chou T T, Yang C N *Phys. Rev.* **170** 1591 (1966)
137. Chou T T, Yang C N *Phys. Rev. Lett.* **20** 1213 (1968)
138. Benecke J et al. *Phys. Rev.* **188** 2159 (1969)
139. Chou T T *Phys. Rev. D* **11** 3145 (1975)
140. Chou T T *Phys. Rev. D* **19** 3327 (1979)
141. Chou T T, Yang C N *Phys. Lett. B* **244** 113 (1990)
142. Krisch A D *Phys. Rev.* **135** B1456 (1964)
143. Islam M M *Nuovo Cimento A* **48** 251 (1967)
144. Cheng H, Wu T T *Phys. Rev. Lett.* **22** 666 (1969)
145. Dias de Deus J *Nucl. Phys. B* **59** 231 (1973)
146. Koba Z, Nielsen H B, Olesen P *Nucl. Phys. B* **40** 317 (1972)
147. Auberson G, Kinoshita T, Martin A *Phys. Rev. D* **3** 3185 (1971)
148. Buras A J, Dias de Deus J *Nucl. Phys. B* **71** 481 (1974)
149. Frahn W E, Venter R H *Ann. Physics* **24** 243 (1963)
150. Frahn W E *Nucl. Phys. A* **302** 267 (1978)
151. Frahn W E *Nucl. Phys. A* **302** 281 (1978)
152. Sprung D W L, Martorell J *J. Phys. A Math. Gen.* **30** 6525 (1997)
153. Sprung D W L, Martorell J *J. Phys. A Math. Gen.* **31** 8973 (1998)
154. Hwa R C *Phys. Rev. D* **22** 759 (1980); *Phys. Rev. D* **22** 1593 (1980)
155. Hwa R C, Zahir M S *Phys. Rev. D* **23** 2539 (1981)
156. Singh V, Roy S M *Phys. Rev. D* **1** 2638 (1970)
157. Uzhinsky V, Galoyan A, arXiv:1111.4984
158. Brogueira P, Dias de Deus J *J. Phys. G Nucl. Part. Phys.* **37** 075006 (2010)
159. Bourrely C, Soffer J, Wu T T *Phys. Rev. D* **19** 3249 (1979)
160. Bourrely C, Soffer J, Wu T T *Phys. Rev. Lett.* **54** 757 (1985)
161. Bourrely C, Soffer J, Wu T T *Eur. Phys. J. C* **71** 1601 (2011)
162. Cudell J-R, Selyugin O V *Phys. Lett. B* **662** 417 (2008)
163. Selyugin O V, Teryaev O V *Phys. Rev. D* **79** 033003 (2009)
164. Selyugin O V, Teryaev O V *Found. Phys.* **40** 1042 (2010)
165. Selyugin O V, arXiv:1205.5867
166. Jenkovszky L L *Riv. Nuovo Cimento* **10** (12) 1 (1987)
167. Kontros J, Kontros K, Lengyel A, hep-ph/0006141
168. Fleming H, Predazzi E *Lett. Nuovo Cimento* **4** 556 (1970)
169. Giffon M, Hama Y, Predazzi E *Z. Phys. C* **25** 129 (1984)
170. Anselm A A, Gribov V N *Phys. Lett. B* **40** 487 (1972)
171. Fiore R et al. *Int. J. Mod. Phys. A* **24** 2551 (2009)
172. Khoze V A, Martin A D, Ryskin M G *Eur. Phys. J. C* **18** 167 (2000)
173. Bertini M et al. *Riv. Nuovo Cimento* **19** 1 (1996)
174. Lukaszuk L, Nicolescu B *Nuovo Cimento Lett.* **8** 405 (1973)
175. Jenkovszky L L, Martynov E S, Struminsky B V *Phys. Lett. B* **249** 535 (1990)
176. Cudell J R, Lengyel A, Martynov E *Phys. Rev. D* **73** 034008 (2006)
177. Martynov E *Phys. Rev. D* **76** 074030 (2007)
178. Donnachie A, Landshoff P V *Phys. Lett. B* **437** 408 (1998)
179. Donnachie A, Landshoff P V, arXiv:1112.2485
180. Goloskokov S V, Kuleshov S P, Selyugin O V *Z. Phys. C* **50** 455 (1991)
181. Donnachie A, Landshoff P V *Phys. Lett. B* **123** 345 (1983)
182. Donnachie A, Landshoff P V *Nucl. Phys. B* **267** 690 (1986)
183. Donnachie A, Landshoff P V *Phys. Lett. B* **185** 403 (1987)
184. Feynman R P, in *High Energy Collisions, Proc. of the Third Intern. Conf., Stony Brook, N.Y.* (Eds C N Yang et al.) (New York: Gordon and Breach, 1969) p. 237
185. Kuraev É A, Lipatov L N, Fadin V S *Sov. Phys. JETP* **45** 199 (1977) [*Zh. Eksp. Teor. Fiz.* **72** 377 (1977)]
186. Balitsky I I, Lipatov L N *Sov. J. Nucl. Phys.* **28** 822 (1978) [*Yad. Fiz.* **28** 1597 (1978)]
187. Gribov L V, Levin E M, Ryskin M G *Phys. Rep.* **100** 1 (1983)
188. Jalilian-Marian J et al. *Nucl. Phys. B* **504** 415 (1997)
189. Balitsky I *Nucl. Phys. B* **463** 99 (1996)
190. Kovchegov Yu V *Phys. Rev. D* **60** 034008 (1999)
191. Kharzeev D, Levin E *Nucl. Phys. B* **578** 351 (2000)
192. Kopeliovich B Z, Potashnikova I K, Povh B, arXiv:1208.5446
193. Cline D, Halzen F, Luthe J *Phys. Rev. Lett.* **31** 491 (1973)
194. Ellis S D, Kislinger M B *Phys. Rev. D* **9** 2027 (1974)
195. Gaisser T K, Halzen F *Phys. Rev. Lett.* **54** 1754 (1985)
196. Afek Y et al. *Phys. Rev. Lett.* **45** 85 (1980)
197. Durand L, Hong P *Phys. Rev. Lett.* **58** 303 (1987)
198. Durand L, Pi H *Phys. Rev. D* **40** 1436 (1989)
199. Margolis B et al. *Phys. Lett. B* **213** 221 (1988)
200. Block M M et al. *Phys. Rev. D* **58** 017503 (1998)
201. Kašpar J et al. *Nucl. Phys. B* **843** 84 (2011)
202. Martin A D et al. *Eur. Phys. J. C* **63** 189 (2009)
203. Ryskin M G, Martin A D, Khoze V A *Eur. Phys. J. C* **71** 1617 (2011); arXiv:1201.6298
204. Martin A D, Khoze V A, Ryskin M G, arXiv:1202.4966
205. Berger E R, Nachtmann O *Eur. Phys. J. C* **7** 459 (1999)
206. Berger E R *Nucl. Phys. B Proc. Suppl.* **74** 96 (1999)
207. Dosch H G, Simonov Yu A *Phys. Lett. B* **205** 339 (1988)
208. Dosch H G, Ferreira E, Krämer A *Phys. Rev. D* **50** 1992 (1994)
209. Bialas A, Bzdak A *Phys. Lett. B* **649** 263 (2007)
210. Bialas A, Bzdak A *Phys. Rev. C* **77** 034908 (2008)
211. Nemes F, Csörgö T, arXiv:1202.2438
212. Carvalho P A S, Menon M J *Phys. Rev. D* **56** 7321 (1997)
213. Ávila R F, Menon M J *Eur. Phys. J. C* **54** 555 (2008)
214. Fagundes D A, Menon M J, Silva G L P *Eur. Phys. J. C* **71** 1637 (2011)
215. Troshin S M, Tyurin N E *Mod. Phys. Lett. A* **27** 1250111 (2012); arXiv:1203.5137
216. Phillips R J N, Barger V *Phys. Lett. B* **46** 412 (1973)
217. Fagundes D A, Menon M J, Silva P V R G, arXiv:1204.5646
218. Cottingham W N, Peierls R F *Phys. Rev. B* **137** B147 (1965)
219. Chou T T, Yang C N *Phys. Rev. Lett.* **20** 1213 (1968)
220. Chou T T, Yang C N *Phys. Rev. Lett.* **46** 764 (1981)
221. Olsen S L *Z. Phys. C* **13** 215 (1982)
222. Dias de Deus J, Kroll P *Acta Phys. Polon. B* **9** 157 (1978)
223. Fischer J, Jakeš P, Novak M *Acta Phys. Polon. B* **14** 807 (1983)
224. Anselm A A, Dyatlov I T *Phys. Lett. B* **24** 479 (1967)
225. Anselm A A, Dyatlov I T *Sov. J. Nucl. Phys.* **6** 430 (1968) [*Yad. Fiz.* **6** 591 (1967)]
226. Khoze V A, Martin A D, Ryskin M G *Eur. Phys. J. C* **18** 167 (2000)
227. Gotsman E, Levin E M, Maor U *Phys. Lett. B* **353** 526 (1995)
228. Andreev I V, Dremin I M, Steinberg D N *Sov. J. Nucl. Phys.* **11** 261 (1970) [*Yad. Fiz.* **11** 468 (1970)]
229. Henyey F S, Tuan R H, Kane G L *Nucl. Phys. B* **70** 445 (1974)
230. Amaldi U, Schubert K R *Nucl. Phys. B* **166** 301 (1980)
231. Henzi R, Valin P *Phys. Lett. B* **48** 119 (1974)

232. Henzi R *Nucl. Phys. B* **104** 52 (1976)
233. Henzi R, Valin P *Nucl. Phys. B* **148** 513 (1979)
234. Henzi R, Margolis B, Valin P *Phys. Rev. Lett.* **32** 1077 (1974)
235. Troshin S M, Tyurin N E *Phys. Lett. B* **707** 558 (2012); arXiv: 1111.4454
236. Landshoff P V, Polkinghorne J C *Phys. Rev.* **181** 1989 (1969)
237. Kroll P *Nucl. Phys. B* **82** 510 (1974)
238. Grein W, Guigas R, Kroll P *Nucl. Phys. B* **89** 93 (1975)
239. Kundrát V, Lokajíek M, Krupa D *Phys. Rev. D* **35** 1719 (1987)
240. Dremin I M *JETP Lett.* **96** 277 (2012) [*Pis'ma Zh. Eksp. Teor. Fiz.* **96** 307 (2012)]
241. Odorico R *Nuovo Cimento A* **54** 96 (1968)
242. Alvarez-Estrada R F *Ann. Physics* **68** 196 (1971)
243. Cahn R *Z. Phys. C* **15** 253 (1982)
244. Martin A *Lett. Nuovo Cimento* **7** 811 (1973)
245. Dremin I M *Nucl. Phys. A* **888** 1 (2012)
246. Dremin I M, Radovskaya A A, arXiv:1209.1935
247. Dias de Deus J, Kroll P *J. Phys. G Nucl. Phys.* **9** L81 (1983)
248. Matveev V A, Muradyan R M, Tavkhelidze A N *Lett. Nuovo Cimento* **7** 719 (1973)
249. Brodsky S J, Farrar G R *Phys. Rev. Lett.* **31** 1153 (1973)
250. Brodsky S J, Farrar G R *Phys. Rev. D* **11** 1309 (1975)
251. Landshoff P V *Phys. Rev. D* **10** 1024 (1974)
252. Mueller A H *Phys. Rep.* **73** 237 (1981)
253. Donnachie A, Landshoff P V *Z. Phys. C* **2** 55 (1979)
254. Donnachie A, Landshoff P V *Z. Phys. C* **61** 139 (1994)
255. Dremin I M, Nazirov M T *Yad. Fiz.* **31** 1606 (1980)
256. Sotiropoulos M G, Sterman G *Nucl. Phys. B* **419** 59 (1994)
257. Sotiropoulos M G, Sterman G *Nucl. Phys. B* **425** 489 (1994)
258. Kwieciǹski J *Phys. Rev. D* **26** 3293 (1982)
259. Kirschner R, Lipatov L N *Z. Phys. C* **45** 477 (1990)
260. Kancheli O V, arXiv:1012.5385